IEEE Access
Multidisciplinary | Rapid Review | Open Access Journal

Date of publication xxxx 00, 0000, date of current version xxxx 00, 0000.

Digital Object Identifier 10.1109/ACCESS.2023.1120000

A Physical Testbed and Open Dataset for Passive Sensing and Wireless Communication Spectrum Coexistence

AHMED MANAVI ALAM[1], (Graduate Student Member, IEEE), MD MEHEDI FARHAD[1], (Graduate Student Member, IEEE), WALAA AL-QWIDER[1], (Graduate Student Member, IEEE), ALI OWFI[2], (Graduate Student Member, IEEE), MOHAMMAD KOOSHA[3], (Graduate Student Member, IEEE), NICHOLAS MASTRONARDE[3], (Senior Member, IEEE), FATEMEH AFGHAH[2], (Senior Member, IEEE), VUK MAROJEVIC[1], (Senior Member, IEEE), MEHMET KURUM[4], (Senior Member, IEEE), AND ALI C. GURBUZ[1], (Senior Member, IEEE)

[1]Department of Electrical and Computer Engineering, Mississippi State University, Mississippi State, MS 39672 USA (e-mail: aa2863@msstate.edu, mf1413@msstate.edu, wq27@msstate.edu, vuk.marojevic@ece.msstate.edu, gurbuz@ece.msstate.edu)
[2]Holcombe Department of Electrical and Computer Engineering, Clemson University, 433 Calhoun Dr, Clemson, SC 29634, USA (e-mail: aowfi@clemson.edu, fafghah@clemson.edu)
[3]Department of Electrical Engineering at the University at Buffalo, Buffalo, NY 14260 USA (e-mail: mkoosha@buffalo.edu, nmastron@buffalo.edu)
[4]School of Electrical and Computer Engineering, the University of Georgia, Athens, GA 30602, United States (e-mail: kurum@uga.edu

Co-first authors: Ahmed Manavi Alam, Md Mehedi Farhad, and Walaa Al-Qwider
Corresponding author: Ali C. Gurbuz (e-mail: gurbuz@ece.msstate.edu).

This work was sponsored by National Science Foundation under Grant No. 2030291, 2047771, 2202972, and 2030157.

ABSTRACT As next-generation communication services and satellite systems expand across diverse frequency bands, the escalating utilization poses heightened interference risks to passive sensors crucial for environmental and atmospheric sensing. Consequently, there is a pressing need for efficient methodologies to detect, characterize, and mitigate the harmful impact of unwanted anthropogenic signals known as radio frequency interference (RFI) at microwave radiometers. One effective strategy to reduce such interference is to facilitate the coexistence of active and passive sensing systems. Such approach would greatly benefit from a testbed along with a dataset encompassing a diverse array of scenarios under controlled environment. This study presents a physical environmentally controlled testbed including a passive fully calibrated L-band radiometer with a digital back-end capable of collecting raw in-phase/quadrature (IQ) samples and an active fifth-generation (5G) wireless communication system with the capability of transmitting waveforms with advanced modulations. Various RFI scenarios such as in-band, transition-band, and out-of-band transmission effects are quantified in terms of calibrated brightness temperature. Raw radiometer and 5G communication samples along with preprocessed time-frequency representations and true brightness temperature data are organized and made publicly available. A detailed procedure and publicly accessible dataset are provided to help test the impact of wireless communication on passive sensing, enabling the scientific community to facilitate coexistence research and quantify interference effects on radiometers.

INDEX TERMS 5G transmission, active-passive spectrum coexistence, deep learning, microwave radiometer, radio frequency interference (RFI), remote sensing.

I. INTRODUCTION

RADIO spectrum, a finite natural resource crucial to various facets of human life, is integral to both active wireless broadband communications transmission and passive Earth observation radiometry [1]–[5]. Our personal and professional lives is dependent on mobile broadband, while applications such as weather forecasting, climate monitoring, astronomy, and space exploration depend critically on the radio spectrum [6]–[12]. The complementary nature of various technologies is evident as they progressively share or operate near the same frequency bands, each with its unique sensitivities, interference tolerances, and usage patterns. The International Telecommunication Union (ITU) defines the Earth Exploration-Satellite Service (EESS) as a radiocommunication service that enables data transmission between earth stations and space stations [13].The main goal of the

EESS is to monitor the conditions of the earth and the atmosphere. This service uses active or passive sensors on satellites to gather crucial information about Earth's characteristics and natural phenomena, including environmental conditions. EESS utilizes the spectrum, which is also essential for various wireless technologies in commerce, transportation, health, science, defense, and the Internet of Things (IoT), highlighting its dual role in both active communication and passive observation needs [14]–[16]. This convergence underscores the interconnected nature of technologies leveraging the radio spectrum for the betterment of humanity.

A radiometer is a specialized instrument in the EESS that plays a pivotal role in remote sensing and Earth observation by measuring naturally occurring thermal radiation. The measured antenna counts are then converted into brightness temperature (T_B) via a calibration algorithm [17]–[19]. This T_B is subsequently translated into various geophysical parameters, including but not limited to soil moisture, atmospheric water vapor, and ocean salinity [20]–[22]. This process allows for monitoring of the environment and climate without direct physical contact. The sensitivity and low noise floor of radiometers are essential characteristics for accurate and reliable data acquisition [23], [24]. This radiometric sensitivity can enable detecting and quantifying even faint signals, indicative of subtle variations in thermal radiation. The low noise floor is essential to discern the weak thermal emissions from the surroundings, enabling the radiometer to capture nuanced changes in the environment. In microwave radiometers, however, challenges arise with Radio Frequency Interference (RFI) when anthropogenic signals such as active wireless communication waveforms contaminate calibrated radiometric T_B measurements of naturally occurring thermal radiation [25]–[29]. RFI, typically non-Gaussian in nature, introduces errors in the sensor's measured data by increasing electromagnetic noise levels, impacting the accuracy of estimates for geophysical variables derived from these measurements [30], [31].

In order to preserve the reliability of these passive sensors, the ITU has taken protective measures, such as allocating specific radio frequency (RF) spectrum bands dedicated to remote sensing and radio astronomy [32]–[35]. This ensures that these critical frequency bands remain free from interference, safeguarding the integrity of radiometric T_B measurements derived from naturally occurring thermal radiation. However, the microwave spectrum continues to be appealing for upcoming wireless networks, including the fifth-generation (5G) wireless communication system. Frequency ranges specifically designated for 5G, like frequency range (FR) 1 (0.45 GHz–6 GHz) and FR2 (24.45 GHz-52.6 GHz), pose potential challenges to protected bands due to issues like out-of-band emissions or unauthorized in-band transmissions [36]–[38].

Efficient methods for detecting, characterizing, and mitigating anthropogenic interference at passive Earth-observing microwave radiometers are imperative [39], [40]. Furthermore, given the growing demand for RF spectrum in mobile broadband communications, finding opportunistic solutions for potential coexistence between stakeholders becomes crucial. This paper presents a physical testbed, housed in an anechoic chamber. It includes a customizable 5G new radio (NR) system capable of transmitting various wireless communication signals and an L-band radiometer similar to those employed in satellite-based Earth exploration for remote sensing. Controlled line-of-sight tests were conducted on the radiometer by exposing it to various types of in-band, transition-band (combination of in-band and out-of-band), and out-of-band emissions. This testbed possesses the capability to produce an extensive dataset featuring diverse transmission attributes, including modulation techniques, frequency band allocations, duty cycles, and power levels, encompassing both in-band, transition-band, and out-of-band setups. The secure environmentally controlled anechoic chamber enabled not only preserving ground-truth information during the experiment but also transmitting signals inside the protected L-band (1400 - 1427 MHz), otherwise illegal to transmit. The data from the testbed experiments can be utilized by researchers to evaluate existing algorithms or to develop new algorithms related to radiometer calibration, RFI detection, classification, identification, mitigation, and spectrum coexistence [25], [41]–[51]. Key contributions of this physical testbed are

- Researchers have access to a publicly accessible diverse dataset featuring L-band microwave radiometers akin to those on Earth observation satellites, which have been subjected to wireless communication waveforms [52], [53]. Additionally, the Python scripts utilized for data preprocessing have been open-sourced, facilitating reproducibility in scientific analyses and advancements in the field.[1]
- The dataset includes various scenarios involving both in-band, transition-band, and out-of-band transmissions that can be used for training RFI detection and mitigation algorithms with a potential to explore coexistence of communication and passive sensing within the same frequency bands.
- The L-band radiometer developed for this study utilizes Software-Defined Radio (SDR), enabling the acquisition of raw in-phase (I) and quadrature (Q) channel samples at 30 MHz bandwidth. This capability proves advantageous for domain transformation, which could be a crucial aspect of spectrum coexistence and RFI detection.
- Ground truth is available in the dataset to evaluate algorithms across the bandwidth with the accessibility of raw in-phase/quadrature (IQ) samples. The experiment scenarios include transmission with different power levels, modulation techniques, and resource allocation.
- Three distinct levels of the received radiometer datasets such as L0 (raw IQ data), L1A (time-frequency repre-

[1]https://github.com/ahmed-manavi/Active_Passive_Spectrum_Coexistence_Testbed_Data.git

sentations of antenna counts), and L1B (calibrated T_B) are developed and shared with the scientific community [53]. Experiments under diverse transmission scenarios allow the differentiation of contamination levels, ranging from obvious/high RFI to subtle/moderate RFI and even cases of undetectable/low contamination.

The present study focuses on the 1400-1427 MHz band, protected under ITU regulations (footnote RR No. 5.340). To ensure compliance and prevent external emissions, experiments were conducted within an anechoic chamber. These constraints to replicate the real-world geometries, but helped us to isolate the system from unknown interference sources. More realistic scenarios are expected to be done outside on shared bands (or unprotected bands). Nonetheless, the current setup still provide critical insights into interference mechanisms and mitigation strategies that are broadly applicable to other frequency bands. In the future, the current setup will extended to the mid-band (i.e., 3200-3400) MHz range. This will facilitate outdoor experiments and the collection of real-world data, further enhancing the applicability and impact of our research on ensuring the coexistence of active and passive sensing systems.

The rest of the paper is organized as follows: Details of the overall testbed, 5G transmission, and radiometer are discussed in Section II. Section III details the experiment scenarios, data attributes, and data pre-processing. Results and Discussions are provided in Section IV and V respectively. Finally, the conclusion is drawn in Section VI.

II. TESTBED

A. OVERALL SETUP

The experimental setup for 5G and radiometer testing was conducted within the controlled environment of an anechoic chamber at Mississippi State University (MSU). As depicted in Figure 1, the configuration included an active 5G signal transmitter and a passive L-band radiometer. The placement of the 5G transmitter antenna and the dual-polarized L-band radiometer receiver antenna ensured a direct line-of-sight between the two components. The 5G transmitter antenna was positioned at the rear of the anechoic chamber, while the radiometer antenna was located at the front. Throughout the experimental procedure, the anechoic chamber's ambient temperature was regulated and maintained at a constant level. Anechoic chambers utilize absorbers to eliminate multi-path and reflected signals, ensuring that radiometer measurements are solely influenced by the environment and directly transmitted 5G waveforms. Radiometer data are also gathered in scenarios where communication transmission is absent, serving as a crucial component for ground truth validation. The schematic diagram depicting both the 5G transmitter and L-band radiometer is presented in Figure 2. A 5G signal generator transmits the waveforms over the air received by the L-band radiometer for further processing. More detailed information regarding the 5G active signal transmission and the passive L-band radiometer receiver can be found in Subsections II-B and II-C respectively.

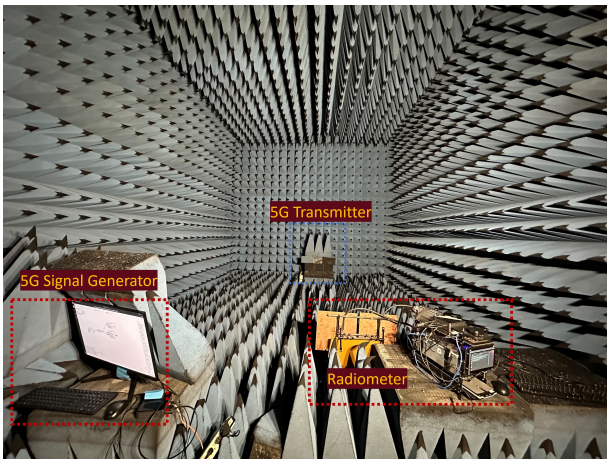

FIGURE 1: Experimental setup illustrating the 5G signal transmitter and L-band radiometer configuration within the anechoic chamber.

B. 5G TRANSMISSION

The transmission side involves encoding, modulation, and signal amplification to ensure reliable and efficient data transfer. Additionally, resource allocation, error correction, and synchronization mechanisms are employed to optimize data transmission, taking into account factors such as bandwidth availability, interference, and noise [54]. Within the domain of the 5G wireless communication system, the transmission architecture is marked by its exceptional speed, ultra-low latency, and massive device connectivity. It leverages advanced modulation schemes, like Quadrature Amplitude Modulation (QAM), and sophisticated error-correcting codes to maximize data throughput and reliability. The system relies heavily on Orthogonal Frequency Division Multiplexing (OFDM) for efficient data transmission and spectral utilization. MIMO technology, in conjunction with beamforming, enhances signal strength, coverage, and spectral efficiency [55].

5G NR stands for the latest radio access technology crafted by the 3rd Generation Partnership Project (3GPP) for the 5G mobile network. The 3GPP offers an exhaustive blueprint of 5G NR through its specification series. In this section, an overview of the frame and carrier structure within 5G NR will be provided, as these concepts bear significance in resource allocation for mobile communication and coexistence. Next, we will introduce the 5G NR OFDM transmission system design employed in this testbed and present an overview of a power measurement experiment under different transmission configurations, providing results for the 5G system alone, without considering the radiometer side.

1) 5G NR frame and carrier structure

The time frame structure in 5G is a designed temporal arrangement that forms the backbone of the system's operation [56]. It provides a framework for transmitting and receiving data. In the context of 5G, the time frame is commonly segmented into intervals of 10 milliseconds (ms) known as

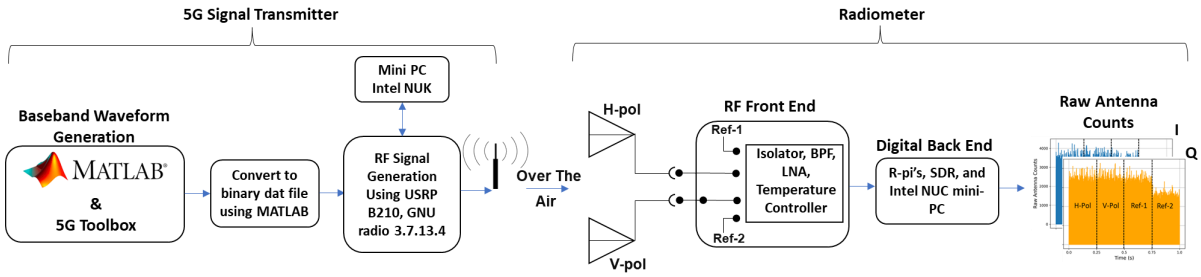

FIGURE 2: 5G-Radiometer Testbed: On the left side, 5G waveforms are transmitted over the air, while on the right side, an L-band radiometer receives signals through its dual-polarized antenna.

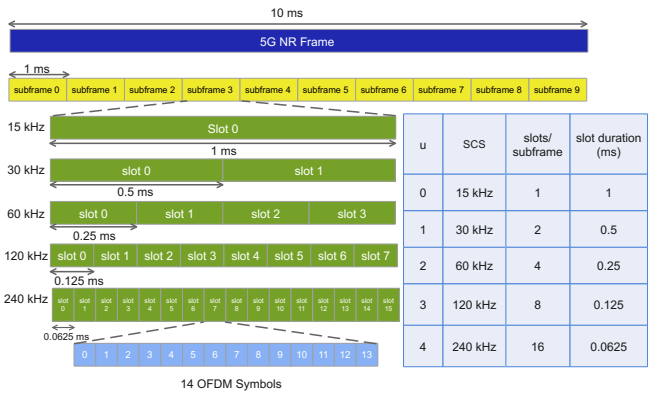

u	SCS	slots/ subframe	slot duration (ms)
0	15 kHz	1	1
1	30 kHz	2	0.5
2	60 kHz	4	0.25
3	120 kHz	8	0.125
4	240 kHz	16	0.0625

FIGURE 3: 5G NR frame structure.

subframes, as depicted in Figure 3. Each subframe, in turn, comprises smaller units called slots, and slots are further divided into OFDM symbols. OFDM symbols are the smallest scheduling units within the time frame structure [56]. 5G NR offers various subcarrier spacing (SCS) options, including 15, 30, 60, 120, and 240 kHz. Numerology dictates the structure of the NR subframe, influencing the number of slots and the duration of OFDM symbols within each subframe. Regardless of the chosen SCS, the subframe maintains a consistent duration of 1 ms [57]. The flexibility to adapt the number of allocated slots, OFDM symbols, and SCS is a key feature in 5G transmitters, offering fine-grained control over the transmission parameters [58]. Our testbed leverages this flexibility to systematically assess the impact of these configurations on radiometric data collected by the adjacent radiometer.

In the frequency domain, 5G networks are characterized by a construct known as the frequency resource grid. This grid spans the entire available frequency band, accommodating different services and transmission requirements. At the finest granularity in this grid is the resource element (RE), which is defined by a subcarrier in the frequency domain and an OFDM symbol in the time domain as illustrated in Figure 4. Multiple REs are grouped to form a resource block (RB), which consists of 12 consecutive REs. The RB is the smallest frequency resource unit that can be allocated to a user within a given transmission time interval (TTI) [59]. This allocation can be dynamically adjusted to meet the varying data needs of different users. Notably, the bandwidth occupied by an RB varies with the chosen SCS, with wider SCS values resulting in broader RBs. RBs are combined into Resource Block Group (RBG) of size P RBs according to the upper layer protocol (the minimum size of P is 2).

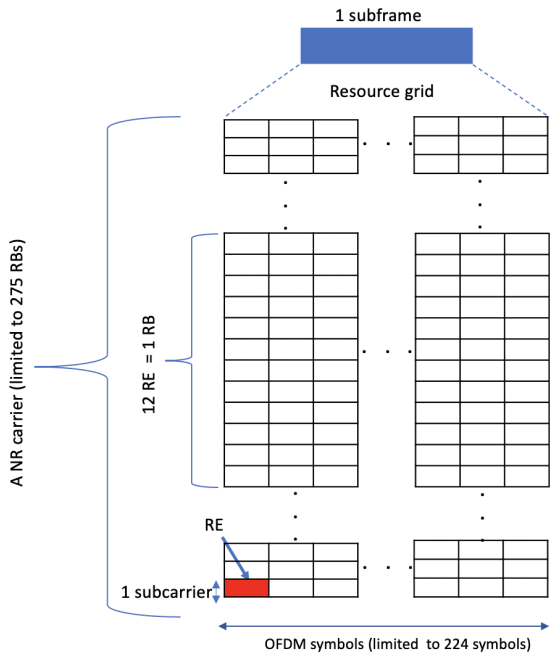

FIGURE 4: 5G NR carrier structure (resource grid).

Within our 5G transmitter design, the ability to allocate and control RBs, subcarrier spacing, and modulation schemes empowers us to investigate the relationship between 5G transmissions and radiometric data reception. By manipulating these parameters, we can systematically assess the impact of 5G transmissions on the frequency resource grid and, subsequently, on the information sensed by the radiometer. Within this time frame structure, the efficiency and performance of data transmission are significantly influenced by the SCS, which dictates the frequency separation between adjacent subcarriers. The choice of SCS, along with other numerology parameters, plays an important role in tailoring the 5G system to meet specific communication requirements, enabling adaptability for diverse use cases such as enhanced

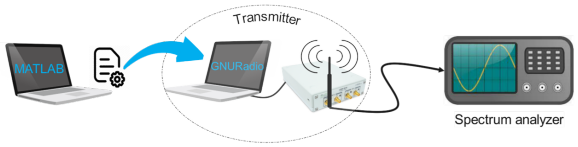

FIGURE 5: 5G received power measurement experiment setup with a wired connection.

mobile broadband (eMBB), massive machine-type communication (mMTC), and ultra-reliable low latency communication (URLLC) [60].

2) 5G NR transmitter design

In the development of the 5G transmitter for our experimental testbed, the MATLAB 5G Toolbox is utilized to create a compliant 5G NR waveform adhering to 3GPP specifications [61]. Using the toolbox functions, we executed transport block generation, OFDM modulation, and the complete waveform generation process. This included downlink shared channel (DL-SCH) encoding, physical downlink shared channel (PDSCH) encoding and modulation, MIMO precoding, and resource grid mapping with subsequent OFDM modulation. Throughout this process, we maintained precise control over critical parameters, including the allocation of RBs, slot, and OFDM symbol allocation within the time frame, as well as power levels, modulation schemes, and coding rates, tailored to suit our experimental requirements. The output of this step comprises the IQ samples, which are converted into binary format using another MATLAB function, preparing them for transmission through GNU Radio and an SDR. To facilitate the transmission of these IQ samples, GNU Radio, an open-source SDR framework, was utilized. GNU Radio provided the essential digital signal processing capabilities required to prepare the waveform for transmission over the airwaves. Its flexibility and extensibility made it an ideal choice for our project. For the experimental phase, National Instrument (NI) Universal Software Radio Peripheral (USRP) B210 device is integrated into our transmission setup. These devices served as interfaces between the antenna and the digital signal processing on our host computer. Chosen with care, the USRP B210 units aligned with our testbed's specifications, offering a wide RF range from 70 MHz to 6 GHz, instantaneous bandwidth of up to 56 MHz, full-duplex transmission capability, and support for multiple-input, multiple-output (MIMO) configurations. To enable over-the-air (OTA) transmission, we integrated cost-effective COTS Proxicast antennas with a 5 dBi gain. These antennas were designed for operation across the frequency bands of interest for our testbed, ensuring compatibility with our experimentation needs.

3) Received power measurement experiment

In this section, we detail the received power measurement analysis conducted solely on the 5G transmission side before proceeding with the complete experiment involving the radiometer. The primary objective of this experiment is to

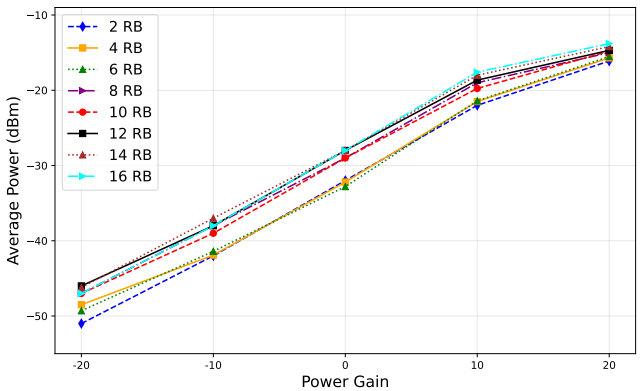

(a)

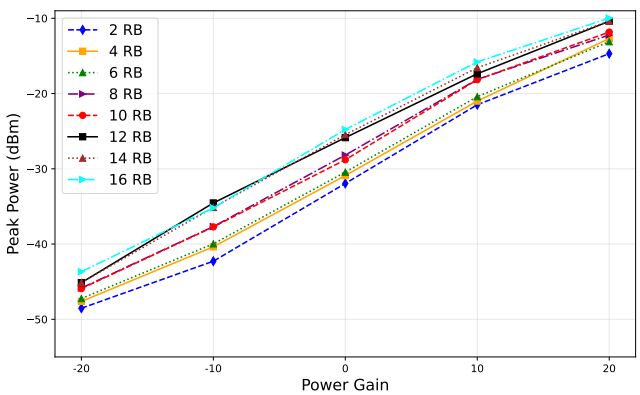

(b)

FIGURE 6: a) Average and b) peak received power measured at the spectrum analyzer for different Matlab gain values and different numbers of RBGs.

validate the actual received power values under varying MATLAB gain settings for different numbers of allocated RBGs. To accomplish this, we employed a spectrum analyzer (SA) as our receiving apparatus to measure the received power level. The SA is connected through a coaxial cable with the transmitter USRP B210, which is connected to the PC executing the GNU radio code for signal transmission as illustrated in Fig 5.

The transmitted IQ waveform is configured with different MATLAB power gain settings and transmitted over varying numbers of RBGs within the available 27 MHz bandwidth. Utilizing a SCS of 15 kHz implies that one RE has a bandwidth of 15 kHz. Given that one RB comprises 12 REs, the bandwidth of one RB is 180 kHz. Consequently, the total number of available RBs amounts to 150 RBs. In our configuration, each RBG comprises 8 RBs, culminating in a collective bandwidth of 1.44 MHz for a specific RBG. Different types of RBG allocations are utilized during the experiment. The average and peak received power, as measured by the spectrum analyzer, are shown in Figure 6a and 6b. These figures demonstrate a clear correlation between increasing gain and a simultaneous rise in both average and peak power. Additionally, a higher number of RBGs is associated with

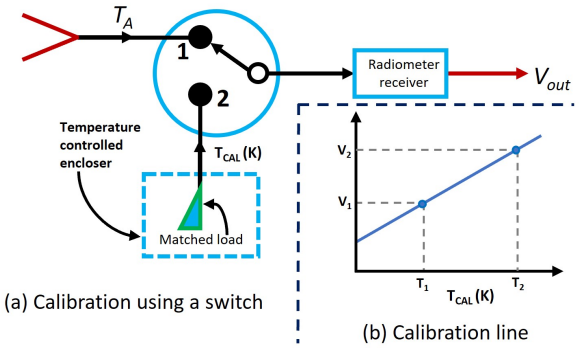

FIGURE 7: Radiometer operation principle [17]

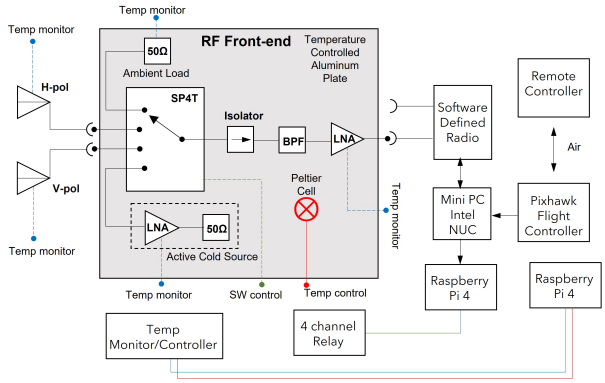

FIGURE 8: Design schematic of a dual-polarized L-band microwave radiometer.

elevated power levels in the received signal. Additional results from our 5G transmitter setup are accessible in our previous publications [62], [63].

C. L-BAND RADIOMETER DESIGN SCHEMATIC

In order to assess the impact of 5G transmissions, a passive receiver in the form of an L-band microwave radiometer has been designed [64]–[67]. The L-band microwave radiometer operates within the safeguarded RF spectrum frequency range of 1400 to 1427 MHz, with a bandwidth spanning 27 MHz. The radiometer does not have any active transmitter, instead, it is a device that provides a quantitative assessment of the intensity of electromagnetic radiation within a specific range of wavelengths in the spectrum. The radiometer measures the natural electromagnetic emissions from a target surface as antenna counts, which are then calibrated to determine the T_B. The translation is achieved by placing two calibration sources using matched load through a switch connected to the input terminal of the radiometer receiver as depicted in Figure 7(a). The output voltage (V_{out}) of the radiometer receiver is linearly related to the noise temperature of the input source. This linear relation is achieved through the radiometer calibration and the resulting calibration line as displayed in Figure 7(b). This allows conversion of V_{out} to the calibrated T_B. The rest of the section describes the radiometer design schematic, compact packaging, receiving antenna design and characterization, and the radiometric calibration to translate the raw IQ samples to T_B.

The hardware architecture of the radiometer is structured into three distinct stages: the design of the RF front-end, the digital back-end processing, and the design and characterization of the dual-polarized array antenna.

1) RF Front-End

The front-end of the radiometer encompasses all RF components, as depicted in Figure 8. Starting with a single-pole four-throw (SP4T) RF relay, the relay's pole can be controlled to enact specific time delays for each through connection via external triggering. The SP4T RF relay utilized in this context demonstrates optimal performance within a frequency band ranging from 1 to 3 GHz. Both the Horizontal polarization (H-pol) and Vertical polarization (V-pol) antennas are connected to the RF relay's 2-port. The remaining two ports of the RF relay are linked to 50-ohm matched loads, fulfilling the roles of an ambient reference load (referred to as a hot source, HS) and a reverse low-noise amplifier (LNA) terminated with a 50-ohm matched load, functioning as an active cold source (ACS). The four ports of the SP4T RF relay are connected with the dual-polarized antenna and reference loads, followed by a 20 dB RF isolator. This RF isolator guarantees unidirectional signal flow while mitigating signal back-propagation. The RF isolator's optimal frequency range lies between 1 GHz to 2 GHz. Subsequently, a custom-designed bandpass (BP) RF filter is connected post-isolator, followed by another LNA. The BP filter operates effectively from 1400 MHz to 1427 MHz, with a center frequency of 1413.5 MHz. The LNA's operational range spans from a minimum frequency of 1.2 GHz to a maximum of 1.6 GHz. To maintain consistent performance, the entire RF front-end is situated on a temperature-controlled aluminum plate, ensuring that the RF components are held at a predefined temperature throughout the operational duration. This temperature control of the RF components serves to minimize stochastic variations in noise levels.

2) Digital Back-End Design

The digital back-end of the radiometer is a critical component of the system, responsible for receiving, processing, and storing the raw radiometric data. The back-end consists of an SDR, Intel's Next Unit of Computing (NUC) mini PC, two Raspberry Pis, and a temperature controller unit. The SDR is a USRP B210 series, which is directly connected to the RF front-end LNA. The SDR digitizes the incoming RF signal at a rate of 30 MHz. The Intel NUC mini PC is responsible for receiving and storing the raw radiometric data from the SDR. One Raspberry Pi is responsible for triggering the SP4T RF relay, which switches the RF signal between the four ports of the radiometer with an integration time of 250 ms. The other Raspberry Pi is responsible for recording the physical temperature of each RF component

TABLE 1: Air-gap patch antenna design parameters.

Parameter	Dimension (mm)	Parameter	Dimension (mm)
Wp	304.00	b	5.00
Lp	320.00	c	25.00
W	65.00	d	15.70
L	74.50	e	49.30
Wf	104.30	f	27.65
Lf	97.00	g	20.00
a	2.00	h	10.00

including the dual-polarized antenna and the coaxial cables. The temperature controller unit uses a Peltier cell to control the temperature of the RF front-end. This is important to minimize temperature drifts, which can affect the accuracy of the radiometric measurements. The digital back-end of the radiometer is a complex system, but it is essential for the accurate and reliable operation of the instrument. The back-end is designed to be flexible and scalable, allowing it to be adapted to a variety of different radiometer applications.

3) Radiometer Multilayered Packaging

The radiometer is packaged in a multilayered box, with the RF components placed on a temperature-controlled aluminum plate. In the radiometer box, the bottom layer holds the RF components, the middle layer contains the SDR, power conversion units, Raspberry Pis, and electromechanical relays, and the top layer holds the temperature controller and power controller for the Peltier cell. Each radiometer component was individually measured with a network analyzer to verify its performance against its specification sheet. After assembling the radiometer, a comprehensive end-to-end radiometric response analysis was conducted using the network analyzer.

4) Antenna Design and Characterization

We have designed and simulated an air gap patch array antenna in an electromagnetic simulation environment. The near-square patch antenna was fabricated on an FR4 substrate (dielectric constant = 4.3, loss tangent = 0.025, thermal conductivity = 0.3 (W/K/m)) with a thickness of 1.47 mm for both the front patch and ground plane. The front and ground planes were made of copper with a thickness of 0.035 mm. An air gap of 8 mm was introduced between the front patch and ground plane to reduce the sidelobe and backlobe levels of the antenna. The design parameters and dimensions are given in Table 1, which corresponds to Figure 9. The antenna feed port was designed with a coaxial SMA connector. The antennas were fabricated using chemical etching and tested with a network analyzer in the anechoic chamber at MSU. Both H-pol and V-pol antennas were attached to a frame for mounting on the unmanned aerial system (UAS).

To minimize sidelobe and backlobe levels, the design of the air gap patch array antenna focused on optimizing the inter-element spacing and the air gap distance between the front patch and ground plane. Figure 10(a) shows the simulated radiation pattern of the antenna. The antenna has a half-power beam width of 37° and a gain of 12.84 dB at the center

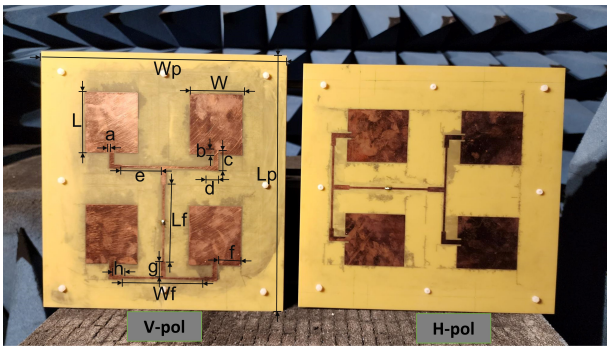

FIGURE 9: V-pol and H-pol air-gap patch antennas were subjected to testing within an anechoic chamber. Both antennas share identical design parameters for their radiating or receiving patches. The ground plane for both antennas comprises an FR4 substrate material with a 1.47 mm thickness, having a 0.035 mm thick copper layer on one side.

frequency of 1413.5 MHz. The theoretical antenna return loss is calculated to be -31 dB in the simulated environment. In the anechoic chamber, the antenna was characterized using a network analyzer and found to have a return loss of -37 dB and -36 dB at the center frequency for H-pol and V-pol antennas, respectively, as shown in Figure 10(b). The solid red line represents the simulated return loss, while the green and blue dotted lines represent the measured return loss for the H-pol and V-pol antennas, respectively.

5) Radiometer Calibration and System Performance

We calibrated the radiometer internal calibration sources using three known external sources: liquid nitrogen (LN), dry ice (DI), and hot source (HS). To assess the stability of calibrated T_B against known external sources, we continuously measured the T_B of a blackbody (the anechoic chamber walls) and the sky for about one hour. We set the radiometer's internal temperature to 305.15 K during the experiment. The blackbody physical temperature (measured with temperature sensors) is shown by the solid black line in Figure 11(a), and the dotted lines show the estimated T_B of the blackbody retrieved with the H-pol and V-pol antennas, respectively. The standard deviation of the estimated T_B for both polarizations was 0.39 K. After this, the antenna was pointed to the sky in an unobstructed environment for about one hour. The estimated T_B of the sky is given in Figure 11(b). The sky T_B is assumed to be 10 K [68], which is the ground truth value. The dotted blue line shows the estimated T_B of the sky measured with the H-pol antenna, and the dotted cyan line represents the V-pol response of the sky T_B. The solid black line is 10 K, the ground truth sky T_B. The standard deviation was calculated to be 0.95 and 0.57 K for H-pol and V-pol, respectively. Although there is a small difference between the sky H-pol and V-pol response, the measurements are already below 1 K. These low standard deviations for the cold sky are expected, as it is well outside of the expected land observation T_B range for which

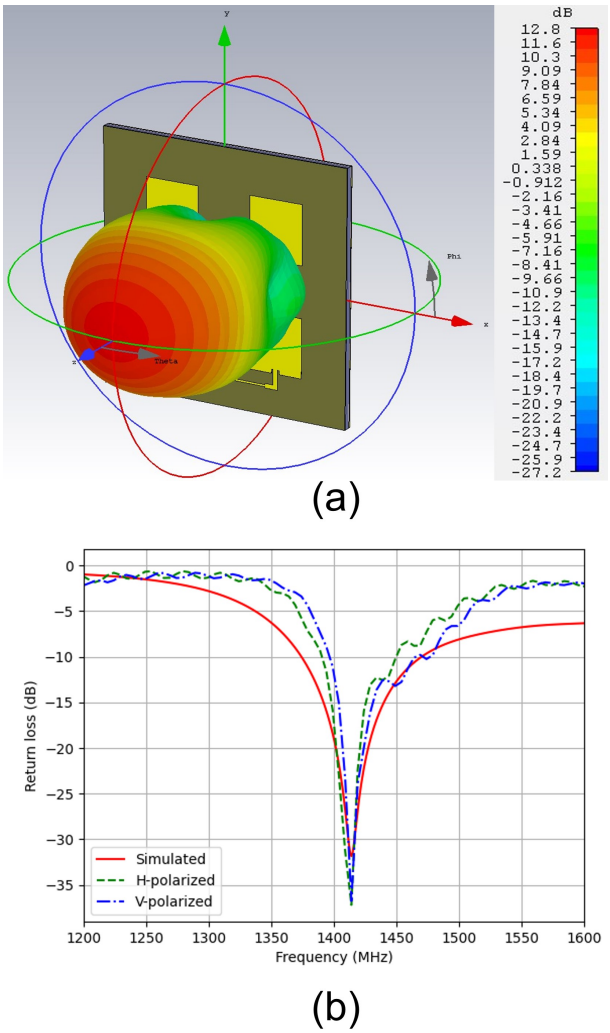

FIGURE 10: (a) 3D simulated radiation pattern of the antenna, (b) the simulated and measured antenna return loss (s_{11}).

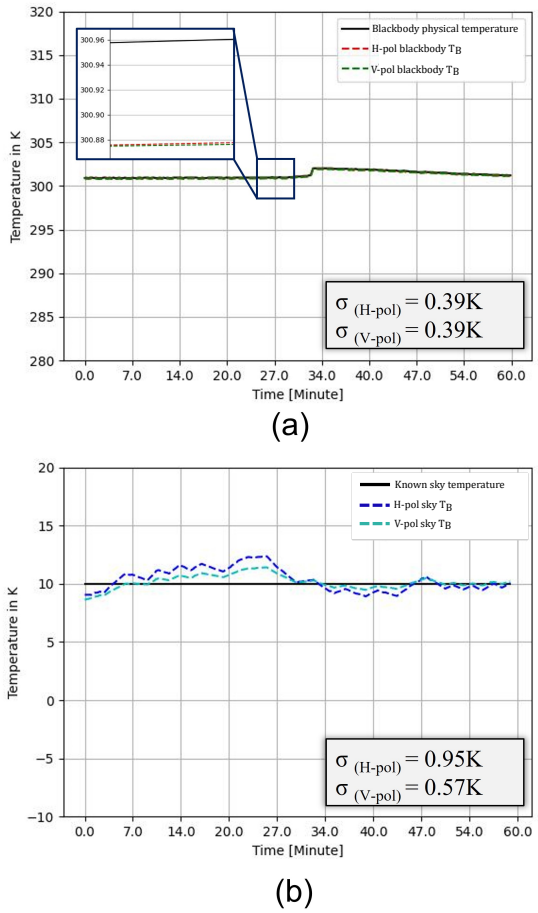

FIGURE 11: Measured and estimated Sky and blackbody temperature with H-pol and V-pol antenna. (a) represents the radiometric T_B response of a blackbody, and (b) represents the measured and estimated sky T_B temperature response using both H-pol and V-pol antenna.

the radiometer is designed and calibrated. The front-end noise figure (NF) in radiometric measurements is driven by the RF components up to the first LNA. For this radiometer, the receiver system noise temperature before the antenna (T_{sys}) is calculated to be 537.1 K, and the corresponding total NF is 4.4 dB using the Y-factor with two known LN and DI sources. The theoretical noise equivalent delta temperature (NEΔT), calculated using T_{sys}, bandwidth B (i.e., 27 MHz), and integration time τ (i.e., 250 ms) is calculated as 0.21 K. The NEΔT is calculated using the ambient blackbody temperature. Additional information regarding radiometer calibration and system performance can be found in the article [64].

III. EXPERIMENTS AND DATASET GENERATION

A. SUMMARY OF EXPERIMENTS

The experimental design comprises distinct scenarios, delineating a comprehensive exploration of the impact of 5G waveforms on radiometric systems. Radiometer acquires IQ samples with a 30 MHz sampling rate. This has been passed through a physical band-pass filter (detailed in Figure 8) to filter out the 1400-1427 MHz portion of the bandwidth with a center frequency 1413.5 MHz (f_{c0}^{o}). To remove high frequency components a Butterworth digital low-pass filter has been designed with a 10 MHz cutoff frequency. This low-pass filter enables the radiometer to a 1405 - 1425 MHz portion of the overall received bandwidth. More details about the data pre-processing are given in Section III-C. Next, the experiments are detailed period.

1) Fully In-band

The initial experiment was designated as in-band transmission where 5G waveforms were intentionally propagated within the operational bandwidth of the radiometer (1400-1427 MHz). This methodology emulates scenarios wherein 5G signals operate within the same frequency range as the

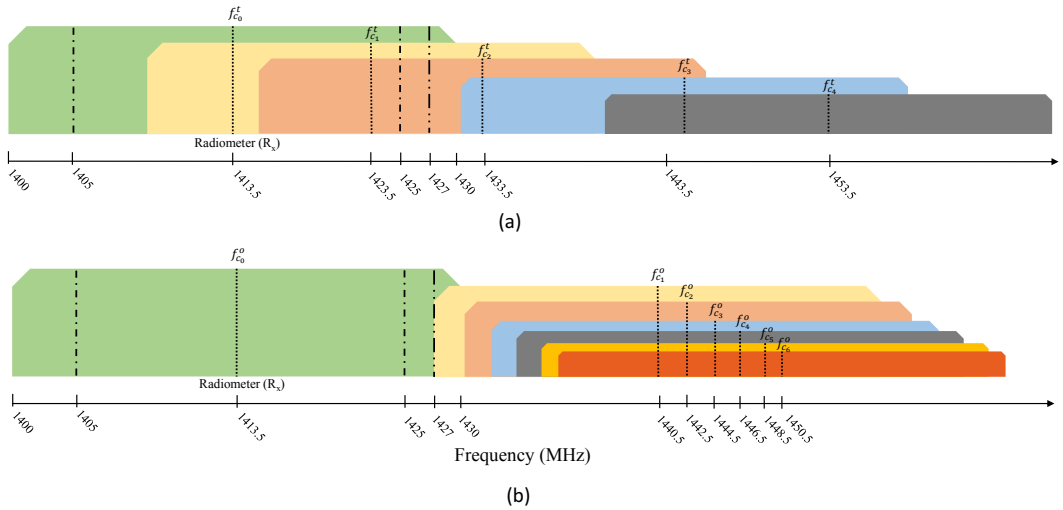

FIGURE 12: Two experiment scenarios with a) transition from in-band to out-of-band emissions and b) fully out-of-band. Radiometer receiver operate within a bandwidth of 30 MHz.

radiometer, facilitating an understanding of in-band transmissions.

2) Transition-Band

In the second experiment illustrated in Figure 12a, 5G waveforms are transmitted with a combination of in-band and out-of-band emissions for the radiometer. Transmitted signals with a center frequency of 1413.5 MHz ($f^t_{c_0}$) demonstrate an in-band transmission. The center frequency of transmitted signals is shifted with a 10 MHz step size spanning from 1423.5 MHz to 1453.5 MHz ($f^t_{c_1}$ $f^t_{c_4}$). This particular experiment is designed specifically to understand the transition effect from a radiometer perspective. Both in-band and transition-band experiments have also been tested with different power gain, RBGs, and modulation techniques. The center frequency of transmitted 5G samples and their corresponding frequency ranges are detailed in Table 2.

3) Out-Of-Band

The subsequent phase of experimentation examines the effects of out-of-band emissions near the radiometer's operating bandwidth. Experiments are conducted to understand this effect, illustrated in Figure 12b. The first experiment demonstrated in Figure 12b involves the transmission of waveforms with distinct center frequencies, spanning a range from 1440.5 MHz to 1450.5 MHz ($f^o_{c_1}$ $f^o_{c_6}$). The center frequency and range of transmitted signals are detailed in Table 2. These frequencies encapsulate a spectrum of values, offering a comprehensive exploration of the effects of out-of-band emissions on the radiometer's operating bandwidth. The intentional selection of six different center frequencies within this range allows for an examination of potential interference and signal interaction with the radiometric system. Out-of-band experiments also consist of samples with different power gain, RBGs, and modulation techniques.

TABLE 2: Experiment scenarios with in-band, transition-band and out-of-band transmissions

Experiment Type	Center Frequency (MHz)	Frequency Range (MHz)
In-band	1413.5	1400-1427
Transition-band	1423.5	1410-1437
	1433.5	1420-1447
	1443.5	1430-1457
	1453.5	1440-1467
Out-of-band	1440.5	1427-1454
	1442.5	1429-1456
	1444.5	1431-1458
	1446.5	1433-1460
	1448.5	1435-1462
	1450.5	1437-1464

4) Varied Gain, Modulation and RBG

Varied gain values, spanning from -20 to 20 dB within 10 10-step increments, were employed during in-band, transition-band, and out-of-band transmissions. In tandem with frequency and gain variations, the experiments incorporate three distinct modulation techniques: Quadrature Phase Shift Keying (QPSK), 16 Quadrature Amplitude Modulation (16QAM), and 64 Quadrature Amplitude Modulation (64QAM). The inclusion of diverse modulation schemes enriches the scope of the study, allowing for a thorough exploration of how different modulation techniques contribute to the observed effects on radiometric measurements. Transmitted signals also consist of different RBG combinations to understand the best resource management approach within an active-passive coexistence framework.

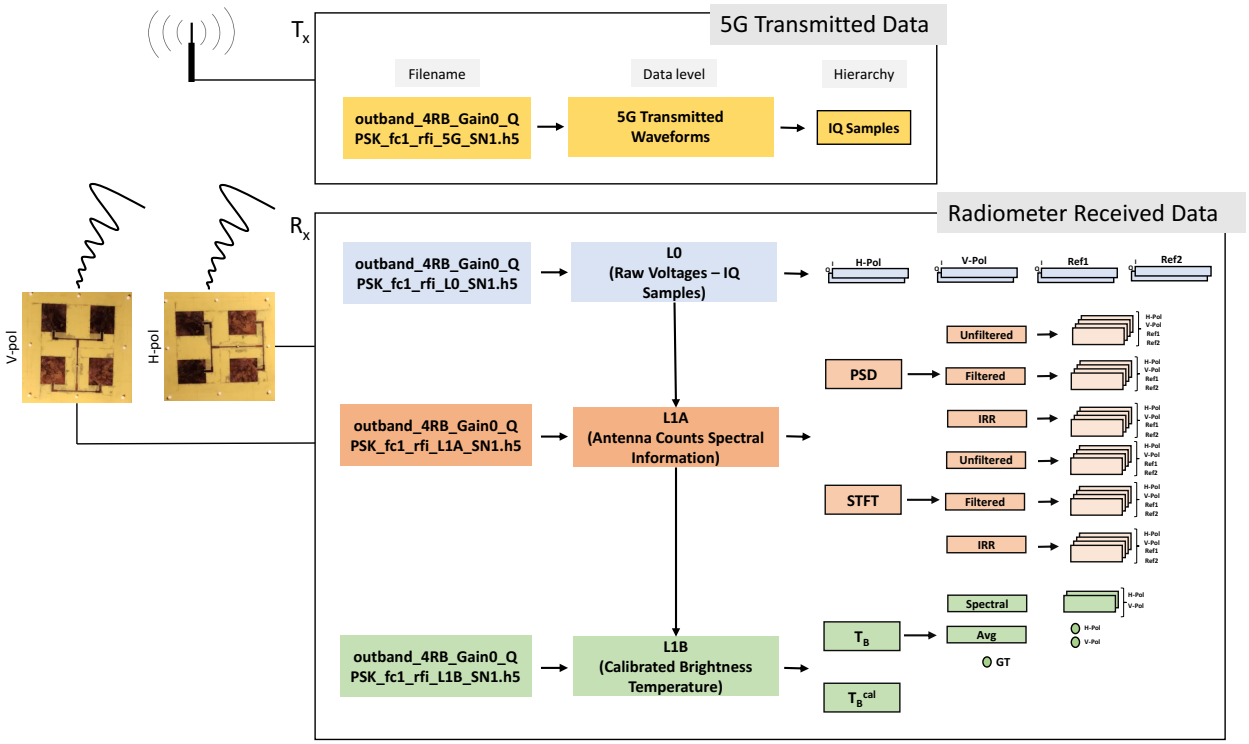

FIGURE 13: Dataset file structure for both transmitted 5G samples and radiometer received data. Raw IQ samples from both the transmitter and receiver are stored as L0 data. Spectral features from radiometer antenna counts are stored as L1A and calibrated T_B are stored as L1B data products.

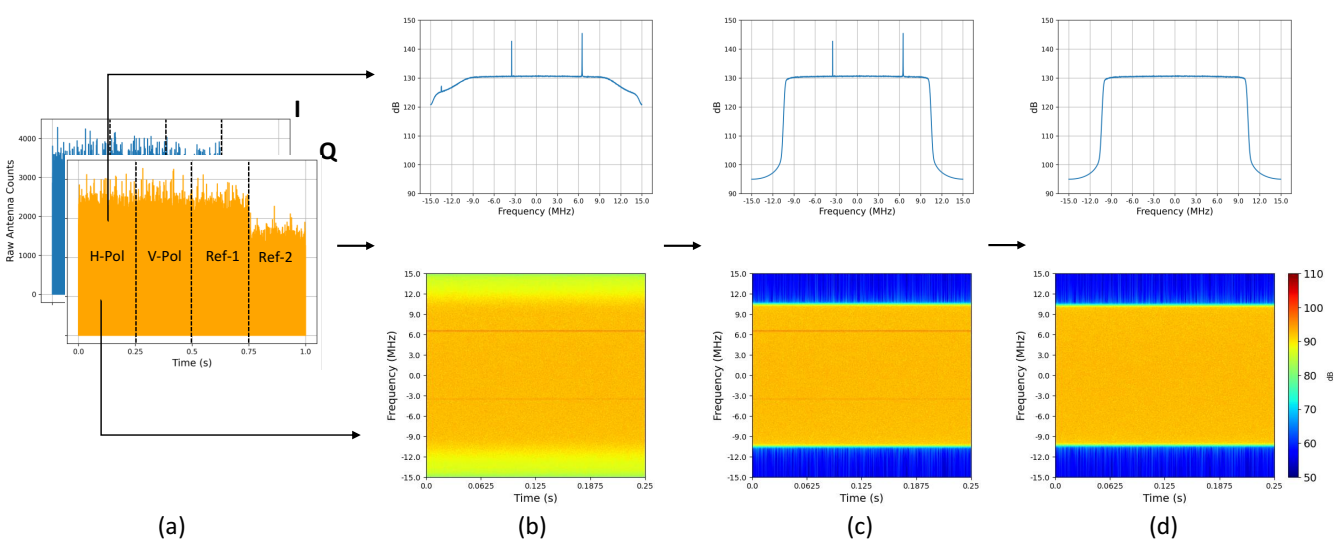

FIGURE 14: Data pre-processing steps for radiometer. a) Raw IQ samples received from the radiometer. A single sample has 1s of integration time with H-pol, V-pol, ref1, and ref2 states. Each state consists of 0.25 s integration time. b) PSD and Spectrograms of received IQ samples before digital filtering, c) after digital filtering, and d) IRR samples.

B. DATASET ATTRIBUTES

In this study, an approach was undertaken to save and share datasets with the scientific community related to 5G-transmitted IQ samples received by a radiometer with different experiment scenarios discussed in the previous section. The dataset for a particular sample comprises four data files, each saved in the hierarchical data format (HDF5) as illustrated in Figure 13 for a specific sample. Transmitted IQ samples of 5G waveforms are saved with necessary information related to RB allocation, modulation technique, and power gain. The radiometer received sample files are categorized into three distinct levels: Level 0 (L0) for raw IQ data, Level 1A (L1A) for antenna counts spectral data, and Level 1B (L1B) for calibrated T_B data. The L0 data encompasses IQ samples divided into H-pol and V-pol polarization, along with reference sources (ref-1 and ref-2) previously described as 'HS' and 'ACS'. The L1A data includes spectral data of raw antenna counts or IQ samples, featuring both Power Spectral Density (PSD) and Short Time Fourier Transform (STFT) data before digital filtering, after digital filtering (between -10 MHz to +10 MHz), and internal RFI removed (IRR) samples. More details about these pre-processing steps are provided in the following subsection. Spectral data are also available in four different states (H-pol, V-pol, ref-1, and ref-2) of the radiometer. To understand the transmitted signal's effects in terms of T_B, the fully calibrated T_B data is available in L1B data. This level encompasses spectral time-frequency T_B features along with average temperature in a particular polarization state. Anechoic room temperature, considered as the ground truth T_B during the transmission, is also recorded. The filenames for each sample are constructed with specific attributes, such as "transmission_band_resource block_PowerGain_ModulationTechnique_SampleNumber". For instance, the filename for an out-of-band transmission with 4 RBGs, 0 gain, and QPSK modulation in the L1B data products is named as "out-band_4RB_Gain0_QPSK_fc1_rfi_L1B_SN1.h5". This systematic naming convention ensures clear identification and organization of the dataset for future analysis and collaboration in the research community.

C. DATA PRE-PROCESSING

Data pre-processing is crucial for testbed data as it enhances the quality and reliability of results by addressing noise, outliers, and inconsistencies, ensuring that the underlying patterns and trends in the data are accurately captured. In this section, a comprehensive workflow to remove any internal bias will be demonstrated. Figure 14a represents IQ samples of a complete cycle (1000 ms) consisting of four segments, each of which represents 250 ms of integrated data. The first two segments are divided into H-pol and V-pol which represent the antenna observation of the scene. The third and fourth segments show the responses of the internal reference loads (Ref-1 and Ref-2 represent the HS and ACS respectively). Figure 14b shows the power spectral density (PSD) and Spectrograms of the uncalibrated raw IQ samples without 5G transmission. These domain transformations illustrate that there are some unwanted biases and spikes located in the radiometer data even when there is no transmission inside the anechoic chamber. Internal electronic and RF instruments might be responsible for causing these unwanted biases in the measurements. To tackle this, a Butterworth low-pass filter with a high order of 28 and a cutoff frequency of 10 MHz is designed to efficiently attenuate higher frequency components, allowing only signals below 10 MHz to pass through with minimal distortion illustrated in Figure 14c. An additional internal RFI detection algorithm has been developed within the filtered region to remove any unwanted bias from the data. An outlier mask has been developed by inspecting 200 different no-RFI (without transmission) samples to find the contaminated frequency bins. The outlier mask has been applied uniformly across all samples to ensure consistency throughout the dataset. IRR samples are depicted in Figure 14d.

D. EVALUATION METRICS TO QUANTIFY EFFECTS OF RFI

This section describes the evaluation metrics employed to quantify the impact of RFI induced by 5G communication waveforms in the L-band radiometer. Both in-band and out-of-band transmissions are observed within a controlled anechoic chamber. The materials utilized in the construction of the anechoic chamber exhibit highly absorbing and non-reflective properties. These materials are designed to possess emissivities close to unity, consequently rendering the radiometer-measured T_B approximately equal to its antenna's physical temperature. The high absorbance and non-reflective nature of the anechoic chamber materials during transmission allow us to attribute observed effects directly to the transmission itself. For both in-band and out-of-band emissions, the impact on the radiometer can be characterized as

$$\Delta T_B = T_{\text{RFI}} \quad T_{\text{No-RFI}} \tag{1}$$

where $T_{\text{No-RFI}}$ is calculated directly from the antenna temperature as the ground truth and T_{RFI} is RFI contaminated T_B estimated with the radiometer internal and external calibration.

IV. RESULTS

In this section, the overall impact on the radiometer will be depicted across three experimental scenarios: fully in-band, transition from in-band to out-of-band, and fully out-of-band. The illustrations will focus on the radiometer's response in terms of ΔT_B. Additionally, the effects of 5G transmitted waveforms will be elaborated, considering various RBGs, power levels, and center frequencies.

A. IN-BAND TRANSMISSION

In the in-band experiment, intentional 5G transmissions were conducted within the 1400 - 1427 MHz bandwidth to assess the radiometer's response within its operational frequency range. This experiment aims to quantify the extent to which electromagnetic radiation is elevated due to 5G transmissions. Figure 15 illustrates the impact on the radiometer (ΔT_B)

across different RBGs and gain levels. The values represent the average effect over a 250 ms integration period for the radiometer. The results clearly indicate that as more RBGs occupy the bandwidth, the overall impact on the radiometer intensifies. Furthermore, higher gain settings for a specific RBG result in a higher ΔT_B compared to other gain levels. This observation substantiates the direct correlation between radiometer T_B and higher RBGs and gain levels.

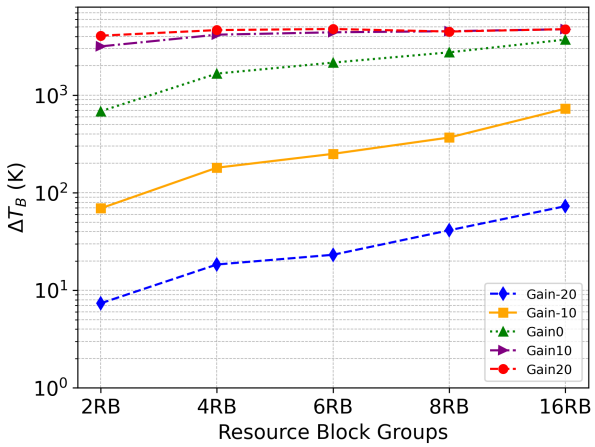

FIGURE 15: Impacts of RFI (ΔT_B) on in-band transmissions considering various signal gains and RBGs for H-pol.

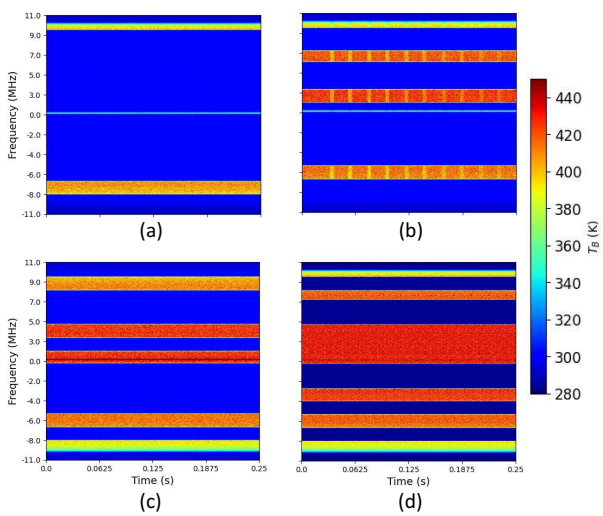

FIGURE 16: Fully calibrated high-resolution spectral T_B in radiometer with in-band transmissions considering Gain -20 with a) 2 RBG, b) 4 RBG, c) 6 RBG, and d) 8 RBG. Recorded ground truth (no-RFI) T_B in this sample is 298.95 K.

For higher gain levels with all RBGs, such as Gain 10 and Gain 20, we can see that the overall effect in the radiometer saturates. The saturation in the radiometer at higher gains (e.g., Gain 10 and Gain 20) stems from multiple key factors. Firstly, at higher gain settings, the radiometer sensor may reach its saturation point, where it becomes incapable of accurately capturing and differentiating variations in signal intensity. This saturation occurs when the sensor's response plateaus, limiting its ability to detect changes in the input signals. Additionally, higher gain levels amplify both desired signals and any accompanying noise or interference, making the system more susceptible to saturation. The radiometer's dynamic range, representing the span between its minimum and maximum detectable signal levels, may also play a role. As gain increases, the system may operate closer to the upper limit of its dynamic range, further contributing to saturation effects. Moreover, non-linearity in the components of the radiometer, especially prevalent at higher gain settings, can introduce distortions in the response, exacerbating the saturation phenomenon. In summary, the saturation observed at higher gain levels reflects a complex interplay of sensor limitations, dynamic range constraints, amplification effects, and system non-linearity within the radiometer. To identify

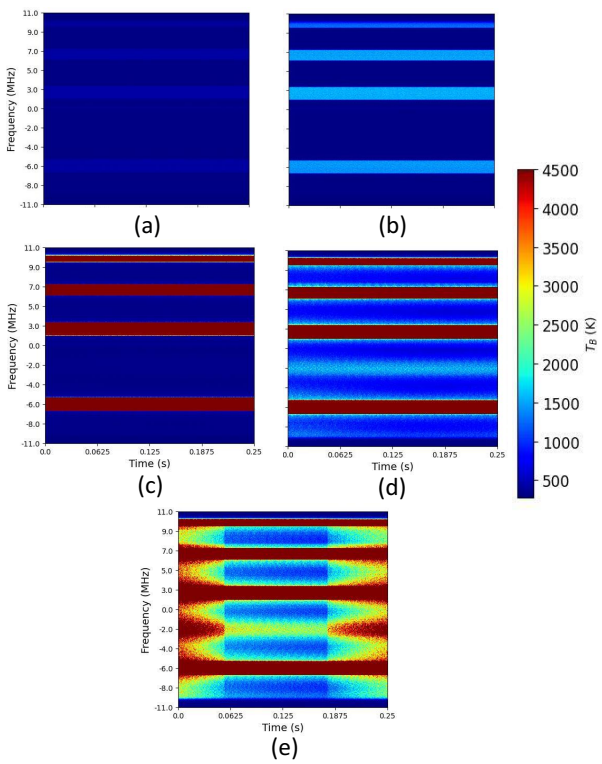

FIGURE 17: Fully calibrated high-resolution spectral T_B in radiometer with in-band transmissions considering 4 RBG with Gain a) -20 b) -10 c) 0, d) 10 and e) 20. Recorded ground truth (no-RFI) T_B in this sample is 298.95 K.

regions within the radiometer bandwidth where the impact of 5G transmission is less intense and potentially usable for passive sensing, we generated high-resolution time-frequency spectrograms in terms of T_B. Figure 16 illustrates the spectral T_B for different RBGs at a specific gain of -20. For a 250 ms integration period in the radiometer, the window size and FFT size for the STFT remained constant at 2048. Consequently, a particular spectrogram for a specific sample comprises approximately 7 million time-frequency bins within

a measurement. In contrast to the total power radiometer, where features are averaged for a specific measurement and integration period, these high-resolution spectral representations offer a wealth of information, potentially crucial for RFI detection, mitigation, and the development of spectrum coexistence frameworks.

Qualitatively, observations from the in-band experiments suggest that configurations with a lower number of RBGs, such as 2 (Figure 16a) or 4 (Figure 16b), exhibit a higher number of non-contaminated portions within the spectrogram, considering a ground truth T_B of 298.95 K. Figure 16c and 16d present high-resolution T_B with 6 and 8 RBGs, revealing power leakage from the occupied bandwidth of RBGs with a particular gain (Gain -20 is utilized for this experiment). This phenomenon could be attributed to imperfect filtering from the transmitter side. Moreover, aggregating emissions from nearby RBGs exacerbates the issue, with more severe effects observed as the number of RBs combined increases. In Figure 17, we present high-resolution T_B variations corresponding to different gain levels for a configuration involving 4 RBGs. It is evident that as transmission power increases with higher gain levels, the radiometer T_B also rises. The impact becomes particularly pronounced within the observed bandwidth of the radiometer as gain levels are elevated (Figures 17d and e). The amplification effects associated with higher gain settings contribute not only to the enhancement of desired signals but also to the amplification of unwanted signals and noise. This phenomenon manifests as power leakage in the transmitted waveforms, as discernible in the radiometer receiver. The RF components of the radiometer and its dynamic range, representing the span between the minimum and maximum detectable signal levels, may further contribute to the saturation observed in the measurements at these higher gain levels. This interplay underscores the importance of carefully considering gain settings for spectrum co-existence frameworks to mitigate potential issues related to signal amplification and dynamic range limitations. The results are presented based on H-pol and QPSK modulation techniques, with similar performance observed for V-pol and other modulation techniques.

B. IMPACT OF TRANSITION-BAND

In this experiment, we assessed the overall effects in the radiometer during the transition from in-band to a fully out-of-band configuration, varying the center frequency (f_c) of the transmitted waveforms. Figure 18 depicts the impact of 5G transmissions with 4 RBG and varying gain settings for different transition center frequencies f_c^t. The figure also includes the radiometer uncertainty, representing the inherent margin of error and variability in measurements. Accurate understanding and quantification of this uncertainty are critical for interpreting observational data reliably. Our measured radiometer uncertainty stands at 0.23 K during this experiment, signifying the minimum detectable change the radiometer can measure. For all gain levels, as transmitted waveforms deviate from the radiometer operating bandwidth, the values of ΔT_B decrease. The impact is more pronounced at higher

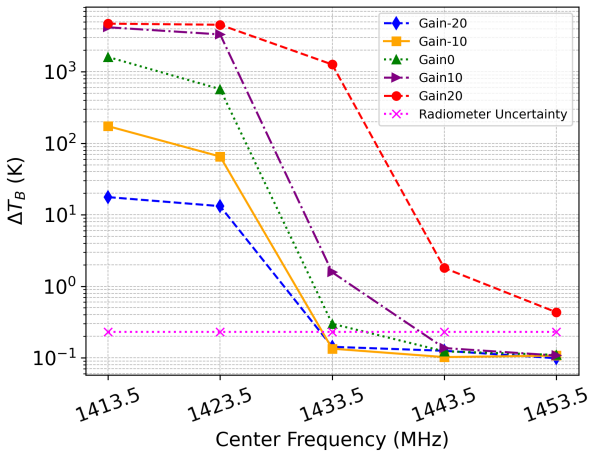

FIGURE 18: Impacts of RFI on a combination of in-band and out-of-band transmissions (transition-band) considering various signal gains and 4 RBG.

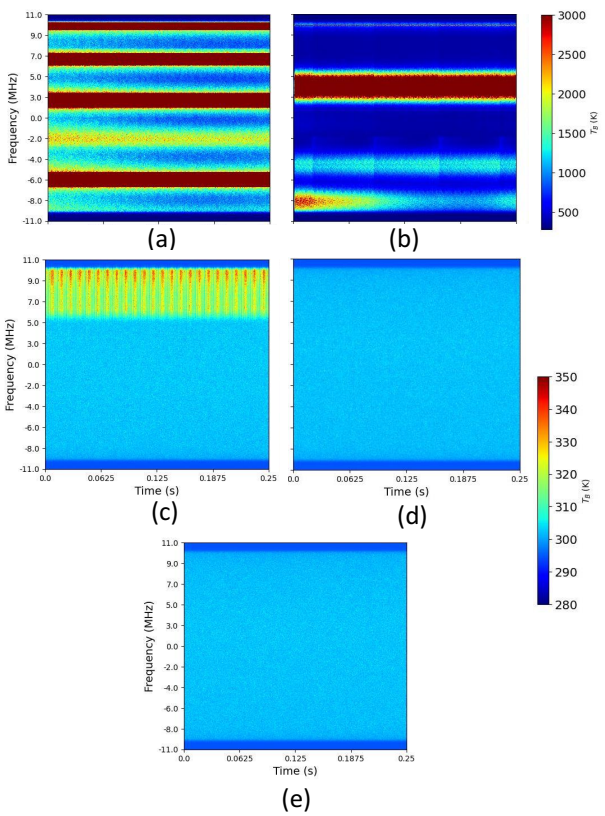

FIGURE 19: Fully calibrated high-resolution spectral T_B in radiometer with transition-band experiment considering 4 RBG with Gain 10 and center frequency of a) 1413.5 MHz ($f_{c_0}^t$), b) 1423.5 MHz ($f_{c_1}^t$), c) 1433.5 MHz ($f_{c_2}^t$), d) 1443.5 MHz ($f_{c_3}^t$) and e) 1453.5 MHz ($f_{c_4}^t$). Recorded ground truth (no-RFI) T_B in this sample is 299.41 K.

gain levels, and ΔT_B saturates with Gain 10 and 20, similar to previous experiments where the transmitted signal fully ($f_{c_0}^t$) and partially ($f_{c_1}^t$) occupied the radiometer bandwidth. During transmission with $f_{c_2}^t$ (center frequency at 1433.5 MHz within an operating frequency range of 1420 - 1447 MHz), higher gains, such as Gain 0, 10, and 20, exhibit impacts exceeding the uncertainty, while Gain -20 and -10 show impacts lower than the uncertainty. This observation may be attributed to lower gain values resulting in reduced leakage power and amplification of unwanted signals and noise. With $f_{c_3}^t$ and $f_{c_4}^t$, the experiment indicates that, except for Gain 20, all other ΔT_B values fall below the radiometer uncertainty. This suggests that lower transmitted power levels result in less leakage in the overall radiometer measurements.

Figure 19 depicts the transition-band spectral T_B with varying center frequencies for four RBG and a Gain of 10. In Figure 12a, transition-band experiment is presented for 5G waveforms with five distinct center frequencies and their corresponding frequency ranges. The transmitted waveforms at $f_{c_0}^t$ can be categorized as fully in-band transmission, as evidenced by the observations in Figure 19a. To quantify the overall impact, ΔT is measured at 4190.605 K for $f_{c_0}^t$. As the transmitted waveform's center frequency deviates from the radiometer, occupying bandwidths with $f_{c_1}^t$ and $f_{c_2}^t$, the overall effects are reduced, as illustrated in Figure 19b and c. Moreover, the overall impact diminishes even further, reaching below the radiometer uncertainty level (0.23 K) for $f_{c_3}^t$ and $f_{c_4}^t$. This observation underscores that transmitted power, specifically associated with Gain 10 and waveforms positioned farther from the radiometer's observation bandwidth, has negligible impact on radiometer observations.

C. OUT-OF-BAND EXPERIMENT

The out-of-band experiment conducted in this study aims to elucidate the effects when portions of the transmitted waveforms intentionally fall outside the protected band designated for remote sensing and radio astronomy (1400 - 1427 MHz). These effects primarily stem from leakage in active transmission bands. Out-of-band transmissions mainly contribute to insidious and undetectable (less than radiometer uncertainty) RFI [25]. This experimental approach holds promise for quantifying these RFI levels. Figure 20 presents the outcomes of the out-of-band experiment across various RBGs and gain levels. ΔT_B of these analysis are associated with radiometer uncertainty to understand the range of undetectable RFI. In the out-of-band experiment, a specific waveform is transmitted with six different center frequencies, as detailed in Section III. Figure 20a provides an overview of the overall effect with 4 RBG and varying gain levels. Except Gain 20, the impact on the radiometer for other gain values remains below the radiometer uncertainty range. This implies the presence of undetectable RFI, given that the radiometer's minimum detectable change is approximately 0.23 K. However, Gain 20, associated with high-power transmission, exhibits a higher ΔT than the radiometer uncertainty across all center frequencies. This underscores that even when 5G waveforms

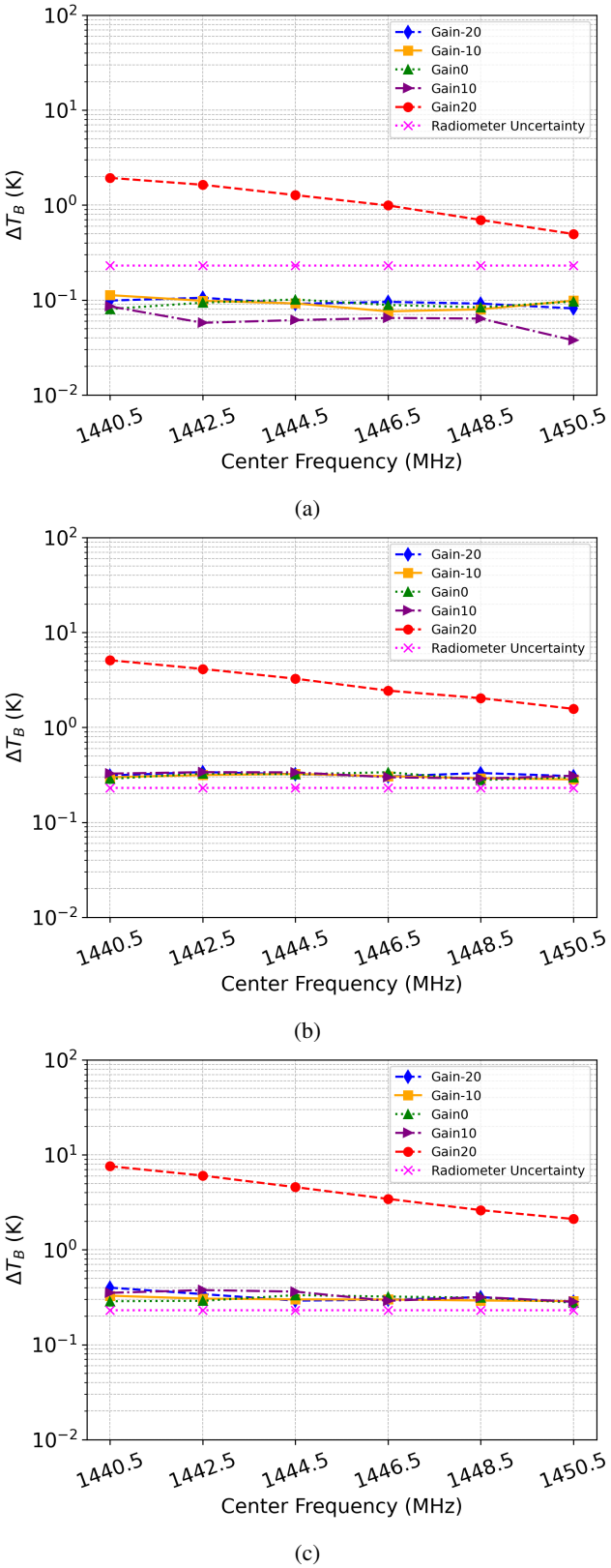

FIGURE 20: Effects of RFI in radiometer with out-of-band transmissions with different center frequencies and a) 4RBG, b) 6RBG, c) 8RBG.

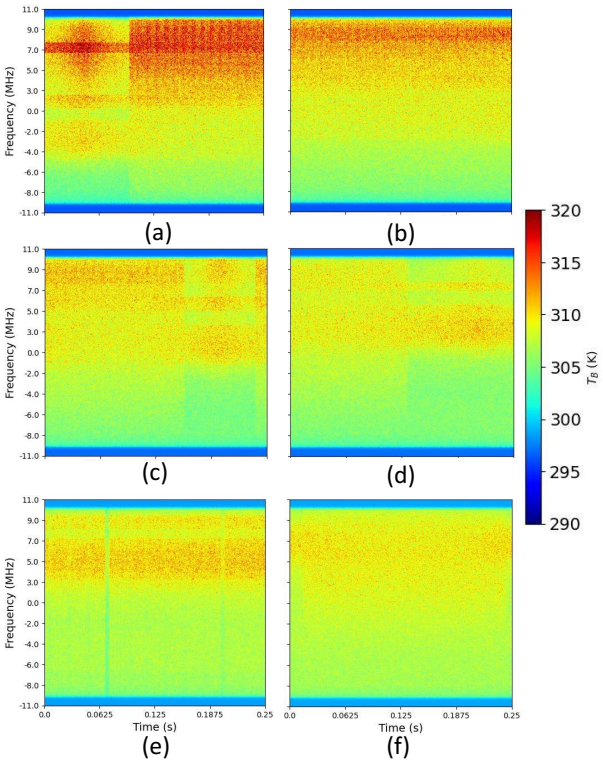

FIGURE 21: Fully calibrated high-resolution spectral T_B in radiometer with out-of-band transmission experiment considering 8 RBG with Gain 20 and center frequency of a) 1440.5 MHz ($f_{c_1}^o$), b) 1442.5 MHz ($f_{c_2}^o$), c) 1444.5 MHz ($f_{c_3}^o$), d) 1446.5 MHz ($f_{c_4}^o$), e) 1448.5 MHz ($f_{c_5}^o$), and f) 1450.5 MHz ($f_{c_6}^o$). Recorded ground truth (no-RFI) T_B in this sample is 299.67 K.

do not transmit within the radiometer operating bandwidth, high power can still significantly impact radiometer measurements.

Figures 20b and c delineate the radiometer impact with 6 and 8 RBGs. For all gain values associated with both RBG configurations, radiometer measurements exhibit contamination. Except for Gain 20, the ΔT_B for 6 RBG ranges from 0.28 to 0.32 K, while for 8 RBG, it varies between 0.31 and 0.35 K. This level of RFI can be characterized as insidious, presenting challenges in detection and quantification. A comparative analysis across RBGs highlights that a higher number of RBG allocations in 5G transmission can exert a substantial impact on radiometer observations. Notably, Gain 20 in conjunction with these three RBG configurations demonstrates significantly elevated ΔT_B, serving as a clear indication that waveforms transmitted with high power are directly correlated with the impact on radiometer observations.

Figure 21 displays the time-frequency spectral T_B with 8 RBG and Gain 20 for six distinct center frequencies in the out-of-band experiment. Sparse hot-spots are discernible across the radiometer time-frequency spectrogram measurements for varying center frequencies. The spectrograms demonstrate that as transmitted waveforms move away from the radiometer-allocated bandwidth, the impacts attenuate. Notably, when the center frequency of transmitted waveforms resides on one side of the spectrum (1427 - 1464 MHz), radiometer observations may remain usable adjacent to the 1400 MHz range. This study demonstrates that radiometer measurements can be contaminated overall, even when 5G transmissions refrain from transmitting inside the protected band.

V. DISCUSSION

This study presents a testbed designed to facilitate research on the coexistence of active wireless communication and passive sensing across various experimental scenarios. The data collected over various distinct scenarios from the testbed has been made publicly available for further analysis and algorithm development by the community. The results obtained from the experimental setups provide valuable insights into the impacts of RFI on passive Earth-observing microwave radiometers, particularly in the context of coexistence with active wireless communication systems such as 5G. During in-band transmission experiments, we observed a direct correlation between the impact of RFI and the number of RBGs as well as different gain levels. Higher RBG occupancy and gain settings led to increased interference, with saturation effects observed at higher gain levels. These results underscore the importance of careful resource and transmission power management to minimize RFI effects on radiometer measurements. Transition-band experiments shed light on the impact of transmissions partially occupying the radiometer's bandwidth. We found that as the center frequency of transmitted waveforms deviated from the radiometer's operating range, the overall interference decreased, highlighting the importance of frequency planning and coordination to mitigate RFI effects. The out-of-band experiments provided valuable insights into the effects of transmissions outside the protected frequency bands designated for passive sensing. Despite not directly transmitting within the radiometer's operating range, high-power transmissions resulted in significant interference, emphasizing the need for robust interference mitigation strategies and spectrum management policies.

Moving forward, our research aims to expand upon these findings by investigating more complex RFI scenarios, including sparse or pulsed interference and different waveform characteristics typical of active technologies. Additionally, we plan to incorporate real-world scenarios by incorporating knowledge from the testbed, considering factors such as path loss and multipath effects. While our study focuses on interference from a single 5G transmitter, it is important to note that this setup does not fully represent the RFI received by spaceborne L-band radiometers, which typically encounter aggregated interference from numerous sources. Future work will explicitly address this by incorporating multiple RFI sources with varying parameters to better simulate real-world conditions. This will provide a more comprehensive understanding of the interference mechanisms and enhance the

relevance of our findings.

Open-sourcing this diverse dataset will empower researchers to assess the effectiveness of existing RFI detection and mitigation models, while also unlocking opportunities to explore the potential of machine learning and computer vision techniques for fostering active-passive spectrum coexistence [69]. This collaborative approach encourages the community to examine deeper into refining RFI management strategies and advancing technologies that facilitate harmonious utilization of the electromagnetic spectrum by both active wireless communication systems and passive sensing applications. While our experiments were conducted in a controlled environment, the knowledge gained from our testbed will be invaluable for understanding and addressing RFI challenges.

VI. SUMMARY AND CONCLUSION

The escalating utilization of diverse frequency bands necessitates the development of efficient methodologies for detecting, characterizing, and mitigating anthropogenic sources of interference. The absence of comprehensive datasets in the domain of active-passive spectrum co-existence poses a significant obstacle to achieving performance enhancements comparable to those witnessed in other domains. To take a step towards addressing this issue, a physical testbed has been presented that integrates a fully calibrated L-band radiometer and a 5G wireless communication system. This testbed is equipped with modulation techniques, including QAM and QPSK. By exposing the radiometer to various in-band, transition-band, and out-of-band transmissions, a diverse dataset has been created that encompasses a wide array of scenarios with ground truth information. This dataset, containing calibrated T_B measured by the radiometer, offers potential reference data for assessing the effectiveness of algorithms in tasks such as detecting and mitigating RFI. Additionally, it will help facilitate research into spectrum co-existence. Many studies rely on simulated datasets for similar purposes, but this real-world data opens pathways to more robust approaches in RFI management and spectrum co-existence strategies.

Our contributions extend to the accessibility of a substantial publicly available dataset, enabling researchers to generate experimental tests for RFI detection and mitigation in radiometers. The scenarios presented also hold the potential to establish communication and passive sensing within the same frequency bands. The use of SDR in the L-band radiometer allows for the acquisition of raw IQ samples, enhancing flexibility for evaluating algorithms across the bandwidth. Moreover, quantifying RFI through in-band, transition-band, and out-of-band transmissions, along with access to ground truth information during signal transmission, enhances our understanding of 5G's impact on microwave radiometers. This methodology allows for the differentiation of contamination levels, ranging from obvious/high contamination to subtle/moderate contamination and even cases of undetectable/low contamination.

In essence, this work presents a dataset for finding a potential solution to the active/passive spectrum co-existence challenge. The developed dataset can also help to quantify the effects of interference on radiometers. The physical testbed and dataset developed in this study are invaluable resources for advancing research in RF domains and fostering the coexistence of active wireless communication and passive sensing technologies.

REFERENCES

[1] I. F. Akyildiz, W.-Y. Lee, M. C. Vuran, and S. Mohanty, "A survey on spectrum management in cognitive radio networks," *IEEE Communications magazine*, vol. 46, no. 4, pp. 40–48, 2008.

[2] M. Cave, C. Doyle, and W. Webb, *Essentials of modern spectrum management*. Cambridge University Press Cambridge, 2007.

[3] Z.-Q. Luo and S. Zhang, "Dynamic spectrum management: Complexity and duality," *IEEE journal of selected topics in signal processing*, vol. 2, no. 1, pp. 57–73, 2008.

[4] S. Talebi, F. Alam, I. Katib, M. Khamis, R. Salama, and G. N. Rouskas, "Spectrum management techniques for elastic optical networks: A survey," *Optical Switching and Networking*, vol. 13, pp. 34–48, 2014.

[5] K. B. Song, S. T. Chung, G. Ginis, and J. M. Cioffi, "Dynamic spectrum management for next-generation dsl systems," *IEEE Communications Magazine*, vol. 40, no. 10, pp. 101–109, 2002.

[6] L. Palen, M. Salzman, and E. Youngs, "Discovery and integration of mobile communications in everyday life," *Personal and ubiquitous computing*, vol. 5, pp. 109–122, 2001.

[7] M. Castells, M. Fernandez-Ardevol, J. L. Qiu, and A. Sey, *Mobile communication and society: A global perspective*. Mit Press, 2009.

[8] E. F. Vermote, D. Tanré, J. L. Deuze, M. Herman, and J.-J. Morcette, "Second simulation of the satellite signal in the solar spectrum, 6s: An overview," *IEEE transactions on geoscience and remote sensing*, vol. 35, no. 3, pp. 675–686, 1997.

[9] C. Giri, E. Ochieng, L. L. Tieszen, Z. Zhu, A. Singh, T. Loveland, J. Masek, and N. Duke, "Status and distribution of mangrove forests of the world using earth observation satellite data," *Global Ecology and Biogeography*, vol. 20, no. 1, pp. 154–159, 2011.

[10] J. W. Waters, L. Froidevaux, R. S. Harwood, R. F. Jarnot, H. M. Pickett, W. G. Read, P. H. Siegel, R. E. Cofield, M. J. Filipiak, D. A. Flower *et al.*, "The earth observing system microwave limb sounder (eos mls) on the aura satellite," *IEEE transactions on geoscience and remote sensing*, vol. 44, no. 5, pp. 1075–1092, 2006.

[11] A. S. Belward and J. O. Skøien, "Who launched what, when and why; trends in global land-cover observation capacity from civilian earth observation satellites," *ISPRS Journal of Photogrammetry and Remote Sensing*, vol. 103, pp. 115–128, 2015.

[12] D. Entekhabi, E. G. Njoku, P. E. O'neill, K. H. Kellogg, W. T. Crow, W. N. Edelstein, J. K. Entin, S. D. Goodman, T. J. Jackson, J. Johnson *et al.*, "The soil moisture active passive (smap) mission," *Proceedings of the IEEE*, vol. 98, no. 5, pp. 704–716, 2010.

[13] M. A. El-Moghazi, J. Whalley *et al.*, *International Radio Regulations*. Springer, 2021.

[14] L. Zhang, Y.-C. Liang, and M. Xiao, "Spectrum sharing for internet of things: A survey," *IEEE Wireless Communications*, vol. 26, no. 3, pp. 132–139, 2018.

[15] A. Jahn, H. Bischl, and G. Heiß, "Channel characterisation for spread spectrum satellite communications," in *Proceedings of ISSSTA'95 International Symposium on Spread Spectrum Techniques and Applications*, vol. 3. IEEE, 1996, pp. 1221–1226.

[16] M. Höyhtyä, A. Mämmelä, X. Chen, A. Hulkkonen, J. Janhunen, J.-C. Dunat, and J. Gardey, "Database-assisted spectrum sharing in satellite communications: A survey," *IEEE Access*, vol. 5, pp. 25 322–25 341, 2017.

[17] D. Long and F. Ulaby, *Microwave radar and radiometric remote sensing*. Artech, 2015.

[18] D. Le Vine, A. J. Griffis, C. T. Swift, and T. J. Jackson, "Estar: A synthetic aperture microwave radiometer for remote sensing applications," *Proceedings of the IEEE*, vol. 82, no. 12, pp. 1787–1801, 1994.

[19] T. Schmugge, P. Gloersen, T. Wilheit, and F. Geiger, "Remote sensing of soil moisture with microwave radiometers," *Journal of Geophysical Research*, vol. 79, no. 2, pp. 317–323, 1974.

[20] T. T. Wilheit and A. Chang, "An algorithm for retrieval of ocean surface and atmospheric parameters from the observations of the scanning multichannel microwave radiometer," *Radio Science*, vol. 15, no. 3, pp. 525–544, 1980.

[21] J. Pulliainen, J.-P. Karna, and M. Hallikainen, "Development of geophysical retrieval algorithms for the mimr," *IEEE Transactions on Geoscience and Remote Sensing*, vol. 31, no. 1, pp. 268–277, 1993.

[22] T. Kawanishi, T. Sezai, Y. Ito, K. Imaoka, T. Takeshima, Y. Ishido, A. Shibata, M. Miura, H. Inahata, and R. W. Spencer, "The advanced microwave scanning radiometer for the earth observing system (amsr-e), nasda's contribution to the eos for global energy and water cycle studies," *IEEE Transactions on Geoscience and Remote Sensing*, vol. 41, no. 2, pp. 184–194, 2003.

[23] R. Newton and J. Rouse, "Microwave radiometer measurements of soil moisture content," *IEEE Transactions on Antennas and Propagation*, vol. 28, no. 5, pp. 680–686, 1980.

[24] D. Le Vine and N. Skou, *Microwave radiometer systems: design and analysis*. Artech, 2006.

[25] S. Misra, P. N. Mohammed, B. Guner, C. S. Ruf, J. R. Piepmeier, and J. T. Johnson, "Microwave radiometer radio-frequency interference detection algorithms: A comparative study," *IEEE Transactions on Geoscience and Remote Sensing*, vol. 47, no. 11, pp. 3742–3754, 2009.

[26] J. R. Piepmeier, J. T. Johnson, P. N. Mohammed, D. Bradley, C. Ruf, M. Aksoy, R. Garcia, D. Hudson, L. Miles, and M. Wong, "Radio-frequency interference mitigation for the soil moisture active passive microwave radiometer," *IEEE Transactions on Geoscience and Remote Sensing*, vol. 52, no. 1, pp. 761–775, 2013.

[27] S. Misra and C. S. Ruf, "Detection of radio-frequency interference for the aquarius radiometer," *IEEE Transactions on Geoscience and Remote Sensing*, vol. 46, no. 10, pp. 3123–3128, 2008.

[28] E. G. Njoku, P. Ashcroft, T. K. Chan, and L. Li, "Global survey and statistics of radio-frequency interference in amsr-e land observations," *IEEE Transactions on Geoscience and Remote Sensing*, vol. 43, no. 5, pp. 938–947, 2005.

[29] J. T. Johnson, A. J. Gasiewski, B. Guner, G. A. Hampson, S. W. Ellingson, R. Krishnamachari, N. Niamsuwan, E. McIntyre, M. Klein, and V. Y. Leuski, "Airborne radio-frequency interference studies at c-band using a digital receiver," *IEEE transactions on geoscience and remote sensing*, vol. 44, no. 7, pp. 1974–1985, 2006.

[30] C. S. Ruf, S. M. Gross, and S. Misra, "Rfi detection and mitigation for microwave radiometry with an agile digital detector," *IEEE transactions on geoscience and remote sensing*, vol. 44, no. 3, pp. 694–706, 2006.

[31] A. M. Alam, A. C. Gurbuz, and M. Kurum, "Smap radiometer rfi prediction with deep learning using antenna counts," in *IGARSS 2022 - 2022 IEEE International Geoscience and Remote Sensing Symposium*, 2022, pp. 8016–8019.

[32] M. Spencer and F. Ulaby, "Spectrum issues faced by active remote sensing: Radio frequency interference and operational restrictions technical committees," *IEEE Geoscience and Remote Sensing Magazine*, vol. 4, no. 1, pp. 40–45, 2016.

[33] C. D. Wende, "Nasa remote sensing missions and frequency issues," in *IGARSS 2000. IEEE 2000 International Geoscience and Remote Sensing Symposium. Taking the Pulse of the Planet: The Role of Remote Sensing in Managing the Environment. Proceedings (Cat. No. 00CH37120)*, vol. 6. IEEE, 2000, pp. 2447–2451.

[34] M. J. Marcus, "Itu wrc-19 spectrum policy results," *IEEE Wireless Communications*, vol. 26, no. 6, pp. 4–5, 2019.

[35] P. De Matthaeis, R. Oliva, Y. Soldo, and S. Cruz-Pol, "Spectrum management and its importance for microwave remote sensing [technical committees]," *IEEE Geoscience and Remote Sensing Magazine*, vol. 6, no. 2, pp. 17–25, 2018.

[36] S. Parkvall, E. Dahlman, A. Furuskar, and M. Frenne, "Nr: The new 5g radio access technology," *IEEE Communications Standards Magazine*, vol. 1, no. 4, pp. 24–30, 2017.

[37] M. Zheleva, C. R. Anderson, M. Aksoy, J. T. Johnson, H. Affinnih, and C. G. DePree, "Radio dynamic zones: Motivations, challenges, and opportunities to catalyze spectrum coexistence," *IEEE Communications Magazine*, 2023.

[38] S. E. Benish, G. H. Reid, A. Deshpande, S. Ravan, and R. Lamb, "The impact of emerging 5g technology on us weather prediction," *Journal of Science Policy & Governance*, vol. 17, no. 2, 2020.

[39] J. Querol, R. Onrubia, A. Alonso-Arroyo, D. Pascual, H. Park, and A. Camps, "Performance assessment of time–frequency rfi mitigation techniques in microwave radiometry," *IEEE Journal of Selected Topics in Applied Earth Observations and Remote Sensing*, vol. 10, no. 7, pp. 3096–3106, 2017.

[40] L. Li, E. G. Njoku, E. Im, P. S. Chang, and K. S. Germain, "A preliminary survey of radio-frequency interference over the us in aqua amsr-e data," *IEEE Transactions on Geoscience and Remote Sensing*, vol. 42, no. 2, pp. 380–390, 2004.

[41] P. N. Mohammed, M. Aksoy, J. R. Piepmeier, J. T. Johnson, and A. Bringer, "Smap l-band microwave radiometer: Rfi mitigation prelaunch analysis and first year on-orbit observations," *IEEE Transactions on Geoscience and Remote Sensing*, vol. 54, pp. 6035–6047, 10 2016.

[42] A. Bringer, J. T. Johnson, Y. Soldo, D. M. L. Vine, P. Mohammed, S. Misra, P. D. Matthaeis, and J. R. Piepmeier, "Properties of the RFI Environment at 1400-1427 MHz as Observed by the Soil Moisture Active/Passive Mission Microwave Radiometer," *IEEE Journal of Selected Topics in Applied Earth Observations and Remote Sensing*, vol. 14, pp. 7259–7267, 2021.

[43] A. Owfi and F. Afghah, "Autoencoder-based radio frequency interference mitigation for smap passive radiometer," in *IGARSS 2023 - 2023 IEEE International Geoscience and Remote Sensing Symposium*, 2023, pp. 6783–6786.

[44] A. M. Alam, M. Kurum, M. Ogut, and A. C. Gurbuz, "Microwave radiometer calibration using deep learning with reduced reference information and 2-d spectral features," *IEEE Journal of Selected Topics in Applied Earth Observations and Remote Sensing*, vol. 17, pp. 748–765, 2023.

[45] M. Ogut, X. Bosch-Lluis, and S. C. Reising, "A deep learning approach for microwave and millimeter-wave radiometer calibration," *IEEE Transactions on Geoscience and Remote Sensing*, vol. 57, no. 8, pp. 5344–5355, 2019.

[46] P. N. Mohammed and J. R. Piepmeier, "Microwave Radiometer RFI Detection Using Deep Learning," *IEEE Journal of Selected Topics in Applied Earth Observations and Remote Sensing*, vol. 14, pp. 6398–6405, 2021.

[47] J. Bradburn, M. Aksoy, P. E. Racette, T. McClanahan, and S. Loftin, "Enabling low-power radiometers with machine learning calibration," in *IGARSS 2022 - 2022 IEEE International Geoscience and Remote Sensing Symposium*, 2022, pp. 7218–7221.

[48] A. M. Alam, M. Kurum, and A. C. Gurbuz, "Radio frequency interference detection for smap radiometer using convolutional neural networks," *IEEE Journal of Selected Topics in Applied Earth Observations and Remote Sensing*, vol. 15, pp. 10 099–10 112, 2022.

[49] A. M. Alam and A. Cafer, "Deep learning based rfi detection and mitigation for smap using convolutional neural networks," in *RFI Workshop 2022*, 2022.

[50] A. M. Alam, M. Kurum, and A. C. Gurbuz, "High-resolution radio frequency interference detection in microwave radiometry using deep learning," in *IGARSS 2023-2023 IEEE International Geoscience and Remote Sensing Symposium*. IEEE, 2023, pp. 6779–6782.

[51] M. Koosha and N. Mastronarde, "Minimizing estimation error variance using a weighted sum of samples from the soil moisture active passive (smap) satellite," in *IGARSS 2023 - 2023 IEEE International Geoscience and Remote Sensing Symposium*, 2023, pp. 772–775.

[52] A. M. Alam, M. M. Farhad, W. Al-Qwider, A. Owfi, M. Koosha, N. Mastronarde, F. Afghah, V. Marojevic, M. Kurum, and A. Gurbuz, "Dataset for spectrum coexistence in passive sensing and wireless communication," 2024. [Online]. Available: https://dx.doi.org/10.21227/968t-td34

[53] A. M. Alam, "Active passive spectrum coexistence testbed data," GitHub repository, 2024. [Online]. Available: https://github.com/ahmed-manavi/Active_Passive_Spectrum_Coexistence_Testbed_Data

[54] W. K. Alsaedi, H. Ahmadi, Z. Khan, and D. Grace, "Spectrum options and allocations for 6g: A regulatory and standardization review," *IEEE Open Journal of the Communications Society*, vol. 4, pp. 1787–1812, 2023.

[55] G. Gür, "Expansive networks: Exploiting spectrum sharing for capacity boost and 6g vision," *Journal of Communications and Networks*, vol. 22, no. 6, pp. 444–454, 2020.

[56] The 3rd Generation Partnership Project (3GPP) "NR; Physical channels and modulation," Technical specification (TS) 38.211, 2022, Version 17.1.0.

[57] W. AlQwider, T. F. Rahman, and V. Marojevic, "Deep q-network for 5g nr downlink scheduling," in *2022 IEEE International Conference on Communications Workshops (ICC Workshops)*, 2022, pp. 312–317.

[58] A. Yazar, B. Peköz, and H. Arslan, "Fundamentals of Multi-Numerology 5G New Radio." 2019.

[59] The 3rd Generation Partnership Project (3GPP) "Physical layer procedures for data," Technical specification (TS) 38.214, 2022, Version 17.1.0.

[60] The 3rd Generation Partnership Project (3GPP), "Study on physical layer enhancements for NR ultra-reliable and low latency case (URLLC)," Technical Report (TR) 38.824, 2019, Version 16.0.0.
[61] T. M. Inc., "Matlab version: 9.13.0 (r2022b)," Natick, Massachusetts, United States, 2022. [Online]. Available: https://www.mathworks.com
[62] W. Alqwider, A. Dahal, and V. Marojevic, "Software radio with matlab toolbox for 5g nr waveform generation," in *2022 18th International Conference on Distributed Computing in Sensor Systems (DCOSS)*, 2022, pp. 430–433.
[63] W. Al-Qwider, A. M. Alam, M. Mehedi Farhad, M. Kurum, A. C. Gurbuz, and V. Marojevic, "Software radio testbed for 5g and l-band radiometer coexistence research," in *IGARSS 2023 - 2023 IEEE International Geoscience and Remote Sensing Symposium*, 2023, pp. 596–599.
[64] M. M. Farhad, A. M. Alam, S. Biswas, M. A. S. Rafi, A. C. Gurbuz, and M. Kurum, "Sdr-based dual polarized l-band microwave radiometer operating from small uas platforms," *IEEE Journal of Selected Topics in Applied Earth Observations and Remote Sensing*, vol. 17, pp. 9389–9402, 2024.
[65] M. M. Farhad, S. Biswas, A. M. Alam, A. C. Gurbuz, and M. Kurum, "Sdr based agile radiometer with onboard rfi processing on a small uas," in *IGARSS 2023 - 2023 IEEE International Geoscience and Remote Sensing Symposium*, 2023, pp. 4368–4371.
[66] M. M. Farhad, S. Biswas, M. A. S. Rafi, M. Kurum, and A. C. Gurbuz, "Design and implementation of a software defined radio-based radiometer operating from a small unmanned aircraft systems," in *2022 IEEE USNC-URSI Radio Science Meeting (Joint with AP-S Symposium)*, 2022, pp. 17–18.
[67] A. M. Alam, M. M. Farhad, M. Kurum, and A. Gurbuz, "An advanced testbed for passive/active coexistence research: A comprehensive framework for rfi detection, mitigation, and calibration," in *2024 United States National Committee of URSI National Radio Science Meeting (USNC-URSI NRSM)*, 2024, pp. 280–280.
[68] E. Dinnat, D. Le Vine, S. Abraham, and N. Floury, "Map of sky background brightness temperature at l-band," *DinnatEtA12010*, 2010.
[69] A. M. Alam, M. M. Farhad, W. AlQwider, V. Marojevic, M. Kurum, and A. C. Gurbuz, "Evaluation of conventional radio frequency interference detection algorithms in the presence of 5g signals in a controlled testbed," in *2024 IEEE International Symposium on Dynamic Spectrum Access Networks (DySPAN)*, Washington, DC, USA, 2024.

AHMED MANAVI ALAM received his B.S. degree in Electrical and Electronic Engineering from Bangladesh University of Engineering and Technology (BUET), Dhaka, Bangladesh in 2019. He is currently working toward the Ph.D. degree in electrical and computer engineering at Mississippi State University, MS, USA. He is currently working as a research assistant at the Information Processing and Sensing (IMPRESS) Laboratory. His research focus includes algorithm development of deep learning-based inverse problems, signal processing, machine learning for remote sensing and physics-aware deep learning. He was a machine learning intern at the High-Performance Computing Collaboratory in Summer 2023. He is a student member of the IEEE Geoscience and Remote Sensing Society (GRSS). He was a finalist at the IGARSS 2022 student paper competition. He was the winner of the Spring 2024 graduate research symposium organized by Mississippi State University. He is a recipient of the National Academy of Sciences (NAS) fellowship.

MD. MEHEDI FARHAD received his B.Sc. degree in Electrical and Electronic Engineering from Ahsanullah University of Science and Technology, Dhaka, Bangladesh, in 2012. He obtained his Ph.D. degree in Electrical and Computer Engineering from Mississippi State University, Mississippi State, MS, USA in May 2024. He is currently working as a postdoctoral research associate at the University of Georgia. He is a recipient of Future Investigators in NASA Earth and Space Science and Technology (FINESST) in 2023. He was a research assistant at the Information Processing and Sensing (IMPRESS) Laboratory. His research interests include investigating Unmanned Aircraft Systems (UAS)-based microwave radiometer, GNSS-R techniques and Unmanned Ground Vehicle (UGV)-based GNSS-T techniques for the remote sensing of Earth surface parameters using low-cost and smart devices. He is a student member of the IEEE and the IEEE Geoscience and Remote Sensing Society (IGRSS).

WALAA AL-QWIDER is a PhD candidate in electrical and computer engineering at Mississippi State University, Starkville, MS, USA. Her research interests include radio resource management, spectrum sharing, wireless testbeds and testing, unmanned aerial vehicle, reconfigurable intelligent surfaces, artificial intelligent and deep reinforcement learning with application to cellular communications.

ALI OWFI is currently a Computer Engineering Ph.D. student at Clemson University. He received his master's and bachelor's degrees in Computer Engineering from Clemson University and Sharif University of Technology, respectively. His research focus is on adaptable and generalized Deep Learning solutions in wireless communication systems. He is interested in Meta Learning, Domain Adaptation, Incremental Learning, as well as wireless interference identification and mitigation.

MOHAMMAD KOOSHA received the B.S. and M.Sc. degrees in electrical and electronics engineering from Isfahan University of Technology (IUT), Isfahan, Iran in 2018 and 2021 respectively. He is currently pursuing his Ph.D. in telecommunication at the University at Buffalo (UB), New York, USA. He is currently working as a graduate research assistant in the Multimedia and Communications and Systems Lab. His research mainly focuses on the spectrum coexistence of the next generation of wireless cellular networks with passive sensing equipment.

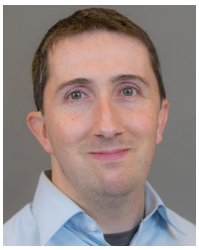

NICHOLAS MASTRONARDE is an Associate Professor in the Department of Electrical Engineering at the University at Buffalo. He received his Ph.D. degree in Electrical Engineering at the University of California, Los Angeles (UCLA) in 2011 and his B.S. and M.S. degrees in Electrical Engineering from the University of California, Davis in 2005 (Highest Honors, Department Citation) and 2006, respectively. He has been the recipient of several awards and honors including a first year department fellowship through the Electrical Engineering department at UCLA, the Dissertation Year Fellowship through the Graduate Division at UCLA, the Dimitris N. Chorafas Foundation Award for 2011, the 2020 SEAS Senior Teacher of the Year Award, and UB's Teaching Innovation Award 2022. He has spent four summers (2013, 2015, 2016, 2018) as a faculty fellow at the US Air Force Research Laboratory (AFRL) Information Directorate in Rome, NY.

Prof. Mastronarde's research interests are in the areas of resource allocation and scheduling in wireless networks and systems, UAV networks, 5G and beyond networks, and reinforcement learning for wireless communications and networking.

FATEMEH AFGHAH is an Associate Professor with the Electrical and Computer Engineering Department at Clemson University and the director of the Intelligent Systems and Wireless Networking (IS-WiN) Laboratory. Prior to joining Clemson University, she was an Associate Professor with the School of Informatics, Computing and Cyber Systems, at Northern Arizona University. Her research interests include wireless communication networks, decision-making in multi-agent systems, UAV networks, security, and artificial intelligence in healthcare. Her recent project involves autonomous decision-making in uncertain environments, using autonomous vehicles for disaster management and IoT security. Her research has been continuously supported by NSF, AFRL, AFOSR, NASA and NIH. She is the recipient of several awards including the Air Force Office of Scientific Research Young Investigator Award in 2019, NSF CAREER Award in 2020, NAU's Most Promising New Scholar Award in 2020, NSF CISE Research Initiation Initiative (CRII) Award in 2017 and Best Paper Award at INFOCOM WiSRAN in 2022. She is the author/co-author of over 150 peer-reviewed publications, and 7 US patents. She served as the associate editor for several journals including ACM Transactions on Computing for Healthcare, Elsevier Journal of Network and Computer Applications, Ad hoc Networks, Computer Networks, and Springer Neural Processing Letters.

VUK MAROJEVIC received the M.S. degree in electrical engineering from Leibniz University Hannover, Hannover, Germany, in 2003, and the Ph.D. degree in electrical engineering from Barcelona Tech-UPC, Barcelona, Spain, in 2009. He is currently an Associate Professor with the Department of Electrical and Computer Engineering, Mississippi State University, Starkville, MS, USA. He is a Principal Investigator of the NSF AERPAW and Open AI Cellular (OAIC) projects. His research interests include cellular network security, O-RAN, spectrum sharing, software radios, testbeds, resource management, and vehicular and aerial communications technologies and systems. Dr. Marojevic is an Editor of the IEEE TRANSACTIONS ON VEHICULAR TECHNOLOGY, an Associate Editor of IEEE Vehicular Technology Magazine, and an Officer of the IEEE ComSoc Aerial Communications Emerging Technology Initiative, and the IEEE VTS AdHoc Committee on Drones.

MEHMET KURUM (M'08–SM'14) received his B.S. degree in Electrical and Electronics Engineering from Bogazici University, Istanbul, Turkey, in 2003, followed by his M.S. and Ph.D. degrees in Electrical Engineering from George Washington University, Washington, DC, USA, in 2005 and 2009, respectively. He held Postdoctoral and Research Associate positions with the Hydrological Sciences Laboratory, NASA Goddard Space Flight Center, Greenbelt, MD, USA. From 2016 to 2022, Dr. Kurum served as an Assistant Professor at Mississippi State University (MSU), and subsequently, he held the position of Associate Professor and the Paul B. Jacob endowed chair until 2023. Currently, he is an Associate Professor in Electrical and Computer Engineering at the University of Georgia, while also serving as an Adjunct Professor at MSU.

Dr. Kurum is a senior member of IEEE Geoscience and Remote Sensing Society (GRSS) and a member of U.S. National Committee for the International Union of Radio Science (USNC-URSI). He serves currently as associate editors for IEEE Transactions on Geoscience and Remote Sensing and IEEE Journal of Selected Topics in Applied Earth Observations and Remote Sensing since 2021. His current research focuses on recycling the radio spectrum to address the challenges of decreasing radio spectrum space for science while exploring entirely new microwave regions for land remote sensing. Dr. Kurum was a recipient of the Leopold B. Felsen Award for excellence in electromagnetic in 2013 and the International Union of Radio Science (URSI) Young Scientist Award in 2014, and NSF CAREER award in 2022. He served as an Early Career Representative for the International URSI Commission F (Wave Propagation and Remote Sensing) from 2014-2021.

ALI GURBUZ received B.S. degree from Bilkent University, Ankara, Turkey, in 2003, in Electrical Engineering, and the M.S. and Ph.D. degrees from Georgia Institute of Technology, Atlanta, GA, USA, in 2005 and 2008, both in Electrical and Computer Engineering. From 2003 to 2009, he researched compressive sensing based computational imaging problems at Georgia Tech. He held faculty positions at TOBB University and University of Alabama between 2009 and 2017 where he pursued an active research program on the development of sparse signal representations, compressive sensing theory and applications, radar and sensor array signal processing, and machine learning. Currently, he is an Assistant Professor at Mississippi State University, Department of Electrical and Computer Engineering, where he is co-director of Information Processing and Sensing (IMPRESS) Laboratory. He is the recipient of The Best Paper Award for Signal Processing Journal in 2013 and the Turkish Academy of Sciences Best Young Scholar Award in Electrical Engineering in 2014, NSF CAREER award in 2021. He has served as an associate editor for several journals such as Digital Signal Processing, EURASIP Journal on Advances in Signal Processing and Physical Communications. He is a senior member of IEEE.